Generation of Multiple Gravity Wave Couplets from Convection

HONGPEI YANG,[a,b,c] YU DU,[a,b,c] AND JUNHONG WEI[a,b,c]

[a] *School of Atmospheric Sciences, Sun Yat-sen University, and Southern Marine Science and Engineering Guangdong Laboratory (Zhuhai), Zhuhai, China*
[b] *Guangdong Province Key Laboratory for Climate Change and Natural Disaster Studies, Sun Yat-sen University, Zhuhai, China*
[c] *Key Laboratory of Tropical Atmosphere–Ocean System, Sun Yat-sen University, Ministry of Education, Zhuhai, China*

(Manuscript received 26 September 2022, in final form 14 July 2023, accepted 18 July 2023)

ABSTRACT: The generation of multiple wave couplets with deep tropospheric downdrafts/updrafts by convection is explored through idealized 2D moist numerical simulations as well as dry experiments with prescribed artificial latent heating. These wave couplets are capable of horizontally propagating over a long distance at a fast speed with vertical motions spanning the entire troposphere. The timing of wave generation is determined by the variation in the local heating rate, which arose from the imbalances among latent heating, nonlinear advection, and adiabatic heating/cooling. The amplitudes of wave couplets also correspond well with the strength of the local heating rate. The heat budget analysis highlights the crucial roles of both latent heating and nonlinear advection in the generation of the tropospheric wave couplets. Strong latent heating induces the thermodynamic imbalance and thus triggers waves. Meanwhile, latent heating also increases vertical motion in the source region and thus enhances nonlinear advection through transferring heat upward. Nonlinear advection, which has a comparable magnitude to latent heating in the upper troposphere, partially offsets the balancing effect of adiabatic heating/cooling, and results in a more persistent imbalance at high levels, allowing for the emission of consecutive waves even when latent heating becomes weak. In the simulation with weak nonlinear advection, fewer wave couplets are found, as the effect of latent heating is more easily offset by adiabatic cooling before it weakens.

SIGNIFICANCE STATEMENT: The generation of gravity waves in the troposphere by convection is of significant importance in the fields of atmospheric science and meteorology. The waves play a crucial role in the initiation and organization of convection, and the parameterization of wave momentum flux in global numerical models. This study aimed to investigate the generation of wave couplets in the troposphere through idealized numerical simulations with varying prescribed latent heating. The results showed that gravity wave couplets were generated in succession as a result of the imbalances among latent heating, nonlinear advection, and adiabatic heating/cooling. This study highlighted an important but yet complex issue of gravity waves being generated within convection by nonlinear sources other than latent heating, which had been neglected in many recent studies on the topic. These findings deepened our understanding of convectively generated gravity waves and paved the way for coupled wave–convection relationship studies.

KEYWORDS: Convection; Gravity waves; Numerical analysis/modeling; Nonlinear dynamics; Latent heating/cooling

1. Introduction

As ubiquitous entities observed in the global atmosphere, gravity waves can be generated by a variety of sources (Fritts and Alexander 2003). Convection, orography, flow imbalance associated with fronts and jets, shear instability, and diurnal land–sea contrast have been documented to generate waves with different characteristics and mechanisms (Durran 1990; Lane and Clark 2002; Plougonven and Zhang 2014; Lane 2015; Wang et al. 2018; Du and Rotunno 2015, 2018; Fang and Du 2022). A great proportion of gravity waves in both the troposphere and middle atmosphere have been shown to be generated by convection through theoretical studies (Nicholls et al. 1991, hereafter NPC91; Beres 2004), observations (Stephan et al. 2016), and numerical simulations (Bretherton and Smolarkiewicz 1989; Lane et al. 2001), and these waves are referred to as "convectively generated gravity waves." Convectively generated gravity waves exert important impacts on the atmosphere. For example, they favor convection initiation (e.g., Su and Zhai 2017; Wilson et al. 2018), organization (e.g., Shige and Satomura 2001; Lane and Zhang 2011), and maintenance (e.g., Stechmann and Majda 2009; Du and Zhang 2019) by changing the cloud environment and providing lifting. A comprehensive understanding of the way in which convection gives rise to gravity waves is fundamental to both finer weather prediction (Du et al. 2021) and realistic parameterizations in current general circulation models (Song et al. 2003; Halliday et al. 2018).

During convection, multiple gravity wave couplets, consisting of alternating downdrafts and updrafts that cover the whole troposphere, are often reported in both observations and simulations (Alexander et al. 2006; Adams-Selin and Johnson 2013; Su and Zhai 2017). These wave couplets encompass a broad spectrum of frequencies with dispersion relation determined by

$$\omega^2 = \frac{N^2 k^2}{k^2 + m^2}, \tag{1}$$

where N is the Brunt–Väisälä frequency. Their angle of energy propagation from the vertical α can be calculated via

Corresponding author: Yu Du, duyu7@mail.sysu.edu.cn

DOI: 10.1175/JAS-D-22-0212.1

$$\cot\alpha = \frac{\omega}{\sqrt{N^2 - \omega^2}}. \tag{2}$$

Hence, low-frequency wave couplets can propagate for a long horizontal distance with little vertical energy escape (Pandya et al. 2000), while high-frequency waves can only travel a limited distance without a trapping/ducting mechanism (e.g., Lindzen and Tung 1976; Ralph et al. 1993; Fovell et al. 2006). As a result, higher-frequency waves triggered in the evolution of convection have been paid less attention in previous studies due to their large vertical component of group velocities.

For wave generation, the *deep heating* mechanism (e.g., Fovell 2002; Beres 2004), which emphasizes the role of diabatic heating in deep convection, has been broadly applied to explain the generation of wave couplets propagating outward from a convective system. Since these deep tropospheric wave couplets mostly feature a maximum amplitude at the midlevel, they are linked to the first vertical mode ($n = 1$, the first baroclinic mode) of the diabatic heating profile (NPC91; Mapes 1993) due to latent heat release. The second baroclinic wave mode ($n = 2$) features opposite vertical movements over the lower and upper halves of the troposphere, and $n = 3$ wave is associated with ascent (descent) in the middle third of the troposphere. The dispersion relation for these waves is calculated assuming hydrostatic balance that

$$\omega^2 = \frac{N^2 k^2}{m^2}, \tag{3}$$

and the horizontal wave speed in an atmosphere at rest, c, can be estimated as

$$c = \frac{ND}{n\pi}, \tag{4}$$

where D denotes the vertical distance between the top of the heating layer and the bottom of the cooling layer, and n represents the wave nodes in the diabatic heating profile. Note that the depth of the heating layer D is roughly equal to the height of tropopause H in deep convection. However, energy leakage to the stratosphere has been found to influence the wave amplitude (Pandya et al. 1993; Halliday et al. 2018). In addition, nonhydrostatic effects (Pandya et al. 1993; Seo et al. 2018) should also be considered when the mechanism is applied to explain waves generated by a shallower convection ($D < H$).

Nonlinear motions within clouds have also been proposed to play a role in generating gravity waves (e.g., Lane 2015). Nonlinear advection associated with buoyancy-driven circulation can perturb the level of neutral buoyancy (LNB) and produce waves at and above the tropopause (e.g., stratosphere) through the *mechanical oscillator* mechanism (Lane et al. 2001). However, the contribution of nonlinear advection to wave generation in the troposphere is not well understood. In Lane and Reeder (2001), it was found that the time scale of nonlinear advection is approximately half of the latent heating time scale, and the two can act to balance or counteract each other. According to (2), the shorter time scales correspond to more vertical propagation of wave energy. Song et al. (2003) found that the effective diabatic forcing and nonlinear forcing are

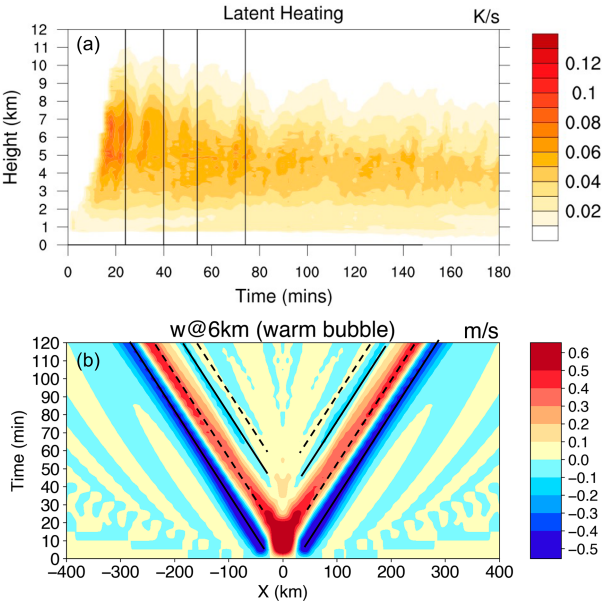

FIG. 1. (a) Multiple $n = 1$ waves' response (downward motion; black lines) to the changes of potential temperature field due to latent heating (shading; K s^{-1}). Adapted from Fig. 5 in Groff et al. (2021). (b) Hovmöller diagram of vertical motion (m s^{-1}) at 6 km AGL in the warm bubble experiment. Black solid and dashed lines indicate the downward and upward motions of $n = 1$ waves, respectively.

comparable but out of phase with each other. In addition, Wang et al. (2018) showed that gravity waves with smaller amplitudes can still appear in their mei-yu front simulation even when latent heating was set to zero in microphysical processes. All of these results suggest the importance of both forcings (latent heating and nonlinear advection) to wave generation, leading to a complex and intriguing question of how these two forcings cooperate in feeding wave generation during convection.

Recent studies by Adams-Selin (2020, hereafter AS20) and Groff et al. (2021) argued that $n = 1$ wave couplets are generated repeatedly due to variations in the latent heating profile during the periodic development of mesoscale convective system (MCS) updrafts. However, the correlation between $n = 1$ waves and latent heating is not always straightforward, as not all peaks in latent heating correspond to $n = 1$ waves (Fig. 1a; adapted from Fig. 5 in Groff et al. 2021), and the wave amplitude is not necessarily proportional to the intensity of latent heating. Does the generation of $n = 1$ gravity waves exactly and directly correspond to the temporal variation in latent heating? Our hypothesis is that other forcings, such as nonlinear advection, may also play a role in the generation of $n = 1$ gravity waves. Through a simple warm bubble dry experiment (a warm bubble vertically occupying the whole troposphere, and only placed in the initial condition), we interestingly found that multiple $n = 1$ gravity wave couplets were still generated, although the amplitude of subsequent waves decreased compared to the first couplet (Fig. 1b). This raises questions about what causes the initial heating (warm bubble) to excite multiple wave couplets and what the main convective processes responsible for wave generation are.

These issues are worth exploring and will be addressed in the present study.

This paper is structured as follows. In section 2, descriptions of the model configuration and the artificial latent heating used in dry experiments are presented. Section 3 describes the convective evolution and associated generating process of gravity wave couplets in the moist simulation. In section 4, artificial latent heating emulating convective generation is used to excite wave couplets in a dry experiment. A detailed heat budget analysis of wave generation is further assessed to explore the mechanisms in this section. Section 5 discusses wave responses to different types of latent heating and system nonlinearity. Conclusions and discussion are presented in section 6.

2. Methodology

a. CM1 configuration for moist experiment

Version 20.3 of the "idealized" Cloud Model 1 (CM1; Bryan and Fritsch 2002) was used to simulate moist deep convection and associated gravity waves. Coriolis force, surface fluxes, and radiative processes were not included in our simulations. The details of the moist simulation (MOIST) design are shown in Table 1. The lateral boundary conditions were open-radiative, while the top and bottom boundary conditions were free-slip. Domain size was 600 km in the x direction, 20 km in the z direction, and 3 km in the y direction (three grids), and the simulation can thus be recognized as a two-dimensional simulation. The time step for model integration was 3 s, with implicit Klemp–Wilhelmson time splitting technique applied vertically to solve pressure. A Rayleigh damping region was incorporated with an inverse e-folding time of 1/300 s^{-1} above 14 km to avoid wave reflection from the model top boundary.

The initial condition of the simulation was obtained by modifying the sounding from Weisman and Klemp (1982). Surface mixing ratio (q_v) at the initial time was set to 14.3 g kg^{-1}, resulting in a maximum unstable convective available potential energy (MUCAPE) value of approximately 2500 J kg^{-1}. No background wind or shear was present to simplify our research due to its effect on wave absorption and dissipation (e.g., Lane and Clark 2002), as well as the asymmetric development of convection (e.g., Rotunno et al. 1988). The environmental stratification profiles are plotted on a skew T–log$p$ diagram in Fig. 2a. Following AS20, Brunt–Väisälä frequency (N) field was calculated and interpolated if anywhere was discontinuous below the tropopause to eliminate possible trapping levels (Fig. 2b). A new potential temperature field was obtained according to the new virtual potential temperature profile retrieved from interpolated N profile with no change to q_v field. To initialize the convection, a warm bubble approach was employed. The Morrison microphysical double-moment parameterization (Morrison et al. 2009) was used with the hail option.

b. Artificial latent heating

To control experiments on how gravity wave couplets were generated through convection without actual phase transition of water, we employed the "toy model" approach (Markowski and Richardson 2014) using a specified heat source to emulate latent heating. Following Beres (2004), the artificial latent heating LH has a Gaussian distribution in the horizontal and a half-sine structure ($n = 1$) in the vertical as

TABLE 1. General CM1 settings and parameter settings for moist and dry experiments.

General settings			
CM1 settings	Value	CM1 settings	Value
Horizontal grid spacing	1000 m	Damping region	>14 km
Vertical grid spacing	250 m	Lateral boundary	Open radiation
Domain extent	600 km × 3 km × 20 km	Top and bottom boundary conditions	Free-slip, zero flux
MOIST	Microphysics scheme	Morrison double moment with hail option on	
	Convection initialization	Warm bubble	

Dry experiment	No microphysics scheme with prescribed latent heating			
	Heating rate amplitude R (K s^{-1})	Temporal variation $Q_t(t)$ (min)	Time of peak heating t_m (min)	Time scale $2\sigma_t$ (min)
CTRL	0.08	$\exp\left[-\left(\frac{t-t_m}{\sigma_t}\right)^2\right]$	15	10
Slow_heat	0.08		15	30
Q_linear	0.0008		15	10
Reinforce_heat	0.08	$\exp\left[-\left(\frac{t-t_{m1}}{\sigma_t}\right)^2\right]+\frac{1}{2}\exp\left[-\left(\frac{t-t_{m2}}{\sigma_t}\right)^2\right]$	15, 30	10
Steady_heat ($0 < t < 50$ min)	0.08	$\frac{2}{\pi}\times\arctan(t_m-\lvert t-t_m\rvert)$	25	–

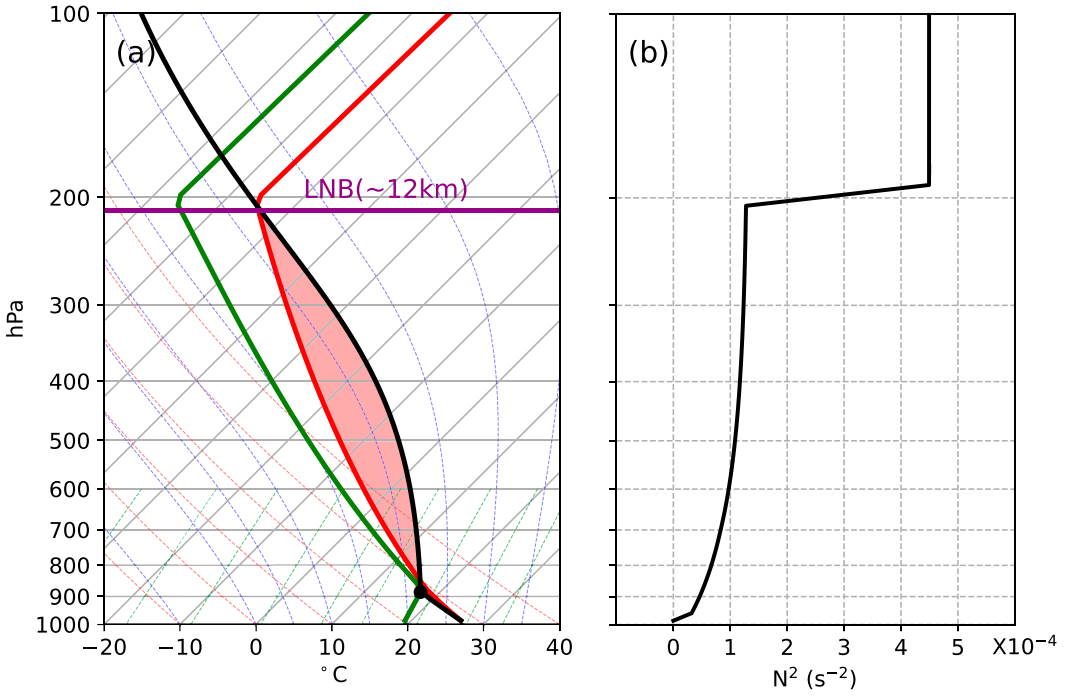

FIG. 2. Environmental thermodynamic profiles used to initialize all model integrations. (a) Skew T–log$p$ diagram of the sounding. The red and green lines represent temperature and dewpoint temperature, respectively. The black line denotes the parcel path and red shaded region indicates CAPE (J kg^{-1}). The level of neutral buoyancy (LNB) is marked with purple line and text. (b) Vertical profile of squared Brunt–Väisälä (N^2) frequency (s^{-2}).

$$\mathrm{LH} = \begin{cases} R\exp\left[-\left(\dfrac{x-x_0}{\sigma_x}\right)^2\right]\sin\left(\dfrac{\pi z}{D}\right)Q_t(t), & 0 \le z \le D, \\ 0, & z > D, \end{cases} \tag{5}$$

where R is the heating rate amplitude. The temporal variation in latent heating $Q_t(t)$ in each experiment is set differently (Table 1), which will be further introduced in section 2c.

The artificial latent heating LH can therefore replace the actual latent variation in the potential temperature tendency equation when moisture is not included:

$$\frac{\partial\theta'}{\partial t} = -u\left(\frac{\partial\theta'}{\partial x}+\frac{\partial\theta_0}{\partial x}\right) - v\left(\frac{\partial\theta'}{\partial y}+\frac{\partial\theta_0}{\partial y}\right) - w\left(\frac{\partial\theta'}{\partial z}+\frac{\partial\theta_0}{\partial z}\right) + \mathrm{LH} + res, \tag{6}$$

where u, v, w, and θ are zonal velocity, meridional velocity, vertical velocity, and potential temperature, respectively, with a superscript prime denoting the perturbation from the base-state value marked by a subscript 0. LH also represents heating and cooling tendencies from microphysical scheme in the moist environment, and the "res" term includes tendencies from moist divergence, turbulence, dissipation, and other optional schemes.

c. Parameter settings for dry experiments

In the control run (CTRL), the moist process was turned off. To reproduce convectively generated gravity waves as in the MOIST in a dry environment, parameters were chosen (Table 1) according to the values simulated in the MOIST experiment. Artificial latent heating was applied with a horizontal scale ($2\sigma_x$) of approximately 10 km in the zonal direction and occupying the entire extent of the troposphere (D = 12 km). The temporal evolution of the latent heating follows a Gaussian distribution with the maximum of heating rate reaching at 15 min, with a heating rate (R) of 0.08 K s^{-1} and a time scale ($2\sigma_t$) of 10 min (red solid line in Fig. 3). Basic parameter values in the MOIST run for CM1 configuration (Table 1) are the same as those in the CTRL run.

Sensitivity experiments were further conducted to explore how wave couplets are generated by convection. As seen in Table 1, most settings for each experiment are the same as those in the CTRL with only one or two settings changed. This method enables us to better understand how wave mechanisms work and make joint contributions to the wave generation. To explore how the temporal variation in latent heating $Q_t(t)$ may influence wave generation, three forms including Gaussian (blue line in Fig. 3), arctangent (green dashed line in Fig. 3), and bimodal (red dotted line in Fig. 3) are used separately in the Slow_heat, Steady_heat, and Reinforce_heat experiments (Table 1). The magnitude of latent heating is reduced in the Q_linear (red dashed line in Fig. 3) to understand the role of nonlinear advection in wave generation. Detailed analysis is presented in sections 4 and 5.

d. Heat budget analysis

Since gravity waves are generated with the aid of buoyancy, analysis of buoyancy variation can be of great importance.

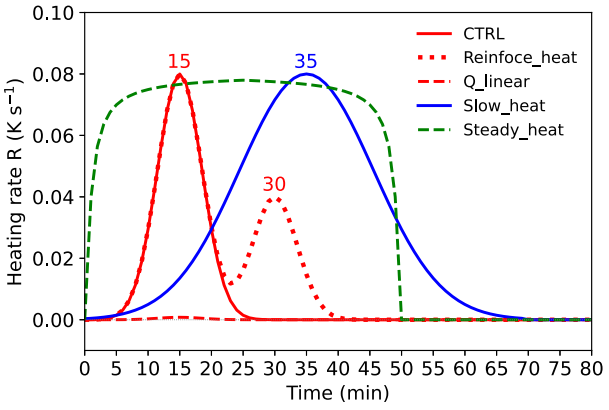

FIG. 3. Schematic of the temporal variation $Q(t)$ of prescribed latent heating rate in five dry simulations. Labels with different colors represent the time when the heating rate reaches a maximum in each simulation.

Equation (6) is the basis for exploring how convective processes influence the variation in potential temperature and buoyancy. As Lane and Reeder (2001) did in their work, we define terms in (6) as follows:

$$\underbrace{\partial\theta'/\partial t}_{\text{local heating rate}} = \underbrace{-u\partial\theta'/\partial x}_{\text{horizontal advection}} \underbrace{-w\partial\theta'/\partial z}_{\text{vertical advection}} \underbrace{-w\partial\theta_0/\partial z}_{\text{adiabatic heating}} + \underbrace{\text{LH}}_{\text{latent heating}} + \text{res},$$

where $-u\partial\theta_0/\partial x$ and $-v(\partial\theta_0/\partial y + \partial\theta'/\partial y)$ are neglected in our research due to the horizontal homogeneity of the base state and application of the two-dimensional simulation. The equation represents the temporal changes of potential temperature perturbation (local heating rate) resulting from horizontal advection, vertical advection, adiabatic heating/cooling, and latent heating due to the phase transition of water in the moist experiment or artificial heat forcing in the dry experiments.

3. Generation of gravity wave couplets by moist convection

a. Evolution of the convection

Established by a warm bubble, a shallow cloud (Fig. 4a) rapidly grows into deep convection at around 22 min (Fig. 4b), with the overshooting top reaching a height of approximately 14 km. Note that the updraft has already reached the LNB (approximately 12 km, Fig. 2a). The intensity of convection is strong, with a maximum updraft exceeding 35 m s^{-1} despite its short-lived longevity and the lack of extra low-level lifting. After 25 min of model integration, the convection starts to decay, characterized by vertical shrinkage of the cloud water and the appearance of a downdraft in Fig. 4c, followed by a weak redevelopment at around 35 min. Interestingly, as shown in Figs. 4c and 4d, clouds at high levels (denoted by the ice water mixing ratio) continue to develop into a broad anvil while the formation of small clouds occurs at middle and low levels. This phenomenon will be explained later in this section.

b. Characteristics of gravity waves

The vertical motions outside the cloud extend the entire depth of the troposphere with a maximum at middle levels and propagate outward from the cloud (Fig. 4). Hovmöller diagram of vertical motion (Fig. 5) further displays similar propagations at different levels (low, middle, and high levels). According to their vertical structure and evolution, such vertical motions belong to $n = 1$ mode of gravity waves (NPC91; AS20). At least three $n = 1$ gravity wave couplets are clearly identified in Fig. 5 (marked by black lines). One wave couplet consists of one branch of downward motion (solid black lines) and the other of upward motion (dashed black lines). Other $n = 1$ wave couplets are not as clear as the first three due to the overlaying of higher wave modes generated concurrently (e.g., $n = 2$ waves with upward motion in the lower troposphere and downward motion in the upper troposphere are generated at the same time with $n = 1$ upward branches, as indicated by green lines in Fig. 5), especially in the vicinity of convection.

The present study focuses on one side of the symmetrical convection development and conducts a detailed analysis of the $n = 1$ wave couplets. Figure 6a provides a close-up view of Fig. 5b to highlight these waves, which exhibit the largest amplitudes at the midlevel. These waves are seen to propagate quickly away from the convective region, with a slightly slower speed near the convective area ($X < 40$ km in Fig. 6a). To analyze their spectral characteristics, a two-dimensional (frequency–horizontal wavenumber) spectrum of the tropospheric vertical motion field is constructed. The black curves in Fig. 7 correspond to the first three tropospheric modes calculated using the dispersion relation (1). The waves close to the convection have two strong power peaks that best fit $n = 1$ curve (Figs. 7a,b), which confirms the dominance of $n = 1$ waves in tropospheric vertical motion field. In a farther region ($X > 40$ km in Fig. 6a), the waves with higher frequency lose energy more significantly due to more vertical propagation (Figs. 7c,d). Generally, the waves that dominate the power spectrum are approximately hydrostatic (Fig. 7), with speeds of 37.45 m s^{-1} (assuming $D = 12$ km, $N = 0.0098$ s^{-1}, $c = ND/n\pi$). The time–height diagram of potential temperature perturbation (θ') and horizontal velocity perturbation (u') at $X = 50$ km (Fig. 6b) further shows the vertical structure of these waves based on the polarization relationship, as the maximum downward (upward) motions are quarter downstream of the maximum (minimum) potential temperature (horizontal velocity) perturbation.

The effects of gravity waves on the cloud environment are also shown in Fig. 6c by taking MUCAPE as an example. It is evident that warming and drying (cooling and moistening) associated with the downward (upward) motion are responsible for the significant decrease (increase) in MUCAPE. For instance, compared with the initial state, the first downward branch of $n = 1$ wave results in a MUCAPE reduction of more than 1000 J kg^{-1} in the vicinity of convection. Nevertheless, the subsequent upward branch with a larger amplitude is able to offset the above reduction in MUCAPE and even destabilize the environment (a MUCAPE increase of ~250 J kg^{-1}). These results are consistent with previous studies (Lane and Reeder 2001;

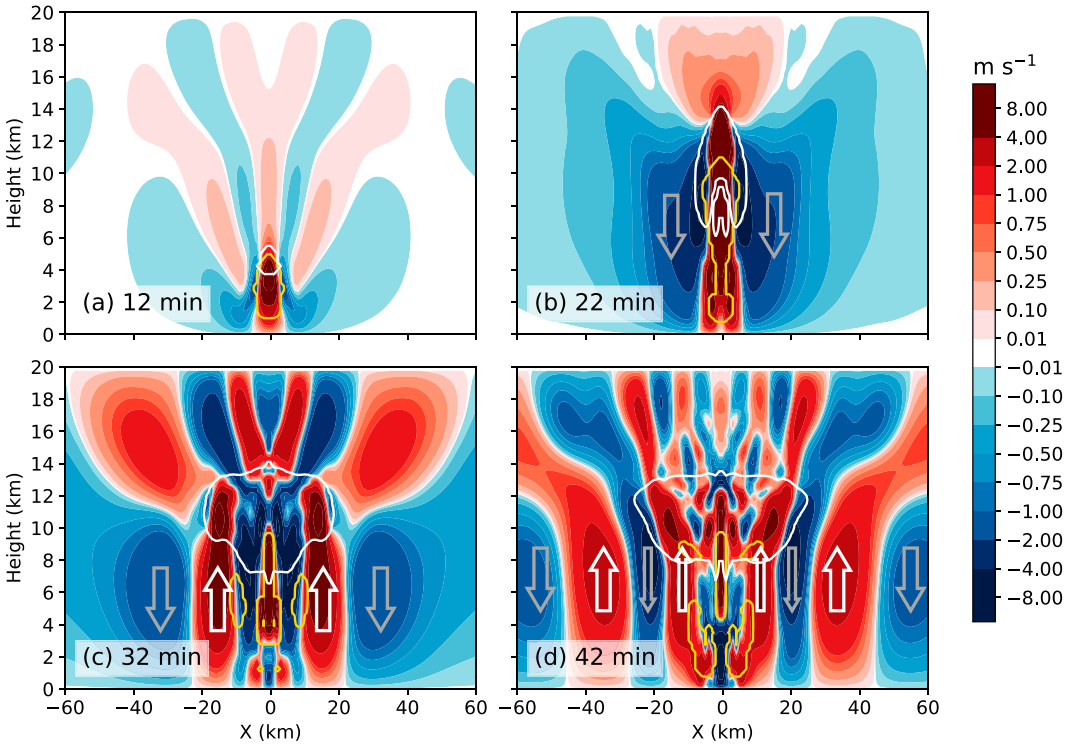

FIG. 4. Temporal evolution of vertical motion (shaded; m s^{-1}), total cloud water (contoured in yellow; 0.01 g kg^{-1}), and ice water mixing ratio (contoured in white; 0.01 g kg^{-1}) at (a) 12, (b) 22, (c) 32, and (d) 42 min for MOIST experiment. Gray and white hollow arrows show downward and upward motions, respectively.

Su and Zhai 2017; AS20), and thus can be used to explain the broadening of cloud anvils and cloud formation mentioned in this section before. New cloud formation is a response to the strong upward motion due to the combination of $n = 1$ and $n = 2$ waves, which is obvious in Figs. 5a and 5b (yellow contours). For the anvil, similarly, its edges also expand outward with waves (Figs. 4c,d and 5b) since ice nucleation might be enhanced by gravity waves (Jensen et al. 2016; Prasad et al. 2019). Therefore, gravity waves can modify the cloud environment and also be beneficial to convection initialization and organization.

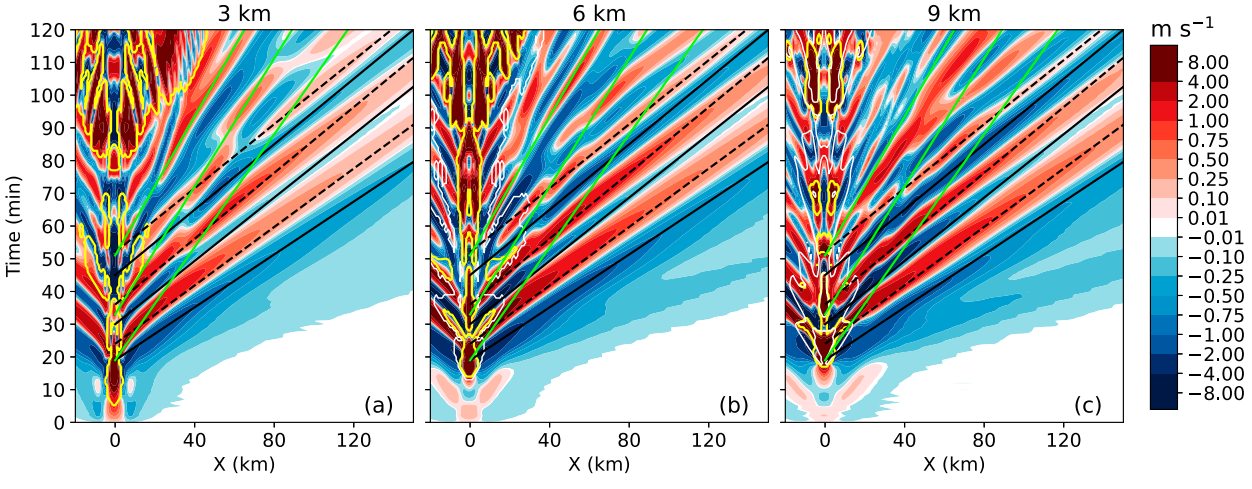

FIG. 5. Hovmöller diagram of vertical motion (m s^{-1}) at (a) 3, (b) 6, and (c) 9 km AGL from the MOIST experiment. Yellow and white contours indicate the cloud water (0.01 g kg^{-1}) and ice crystal (0.01 g kg^{-1}) mixing ratio at each level. Black solid and dashed lines indicate the downward and upward motions of $n = 1$ wave couplets, and green solid lines indicate possible $n = 2$ waves accompanied by upward motions of $n = 1$ waves.

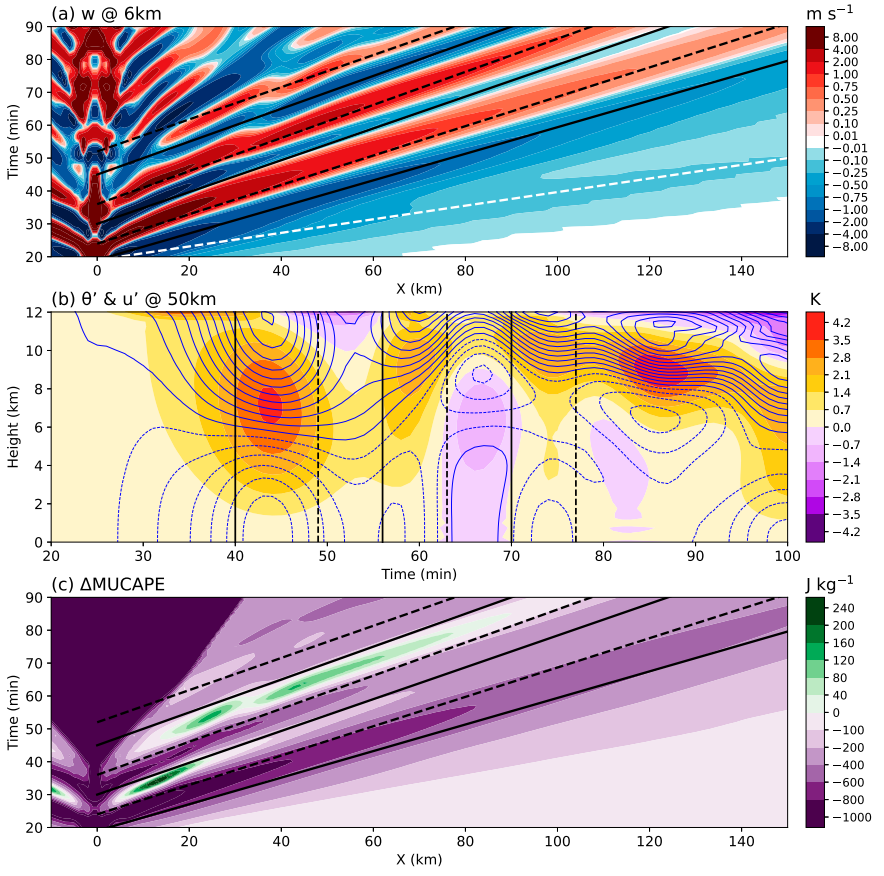

FIG. 6. Hovmöller diagram of (a) vertical motion (m s^{-1}) at 6 km AGL. White dashed line in (a) represents a fake numerical wave. Black solid and dashed lines indicate the downward and upward motions of $n = 1$ wave couplets, respectively. (b) Time–height diagram of potential temperature perturbation (shading; K) and horizontal velocity perturbation (contours in blue, with an interval of 1 m s^{-1} and negative values dashed) at $X = 50$ km. (c) As in (a), but for the change in MUCAPE (J kg^{-1}) from the initial background state.

c. *The generation of wave couplets*

Gravity wave couplets studied in the present study are related to the main updraft (i.e., these waves are convectively generated), as seen in both Figs. 4 and 5. To explore the wave generation processes, it is necessary to exclude unrealistic gravity waves in simulations. In Fig. 6a, a faster propagating downward motion (white line, $c \sim 75$ m s^{-1}) accompanied by the first $n = 1$ downward branch is noted. One possibility is the "fast-mode" mass adjustment discussed in Haertel et al. (2001). However, sensitivity tests increasing the vertical depth of the model show that the wave signal is remarkably weakened, characterized by decreased amplitude and increased speed (figure not shown), which suggests another possibility is that the response of $n = 1$ wave to the entire vertical simulation domain may not be representative of what would occur in an actual atmosphere without a top boundary.

Our main purpose is to examine the detailed processes of wave generation, in particular for $n = 1$ wave couplets due to their high visibility in short-lived convection without vertical shear. The generation mechanisms of higher-order waves in long-lived convection with vertical shear will be explored in future studies. A crucial question is when these $n = 1$ waves are generated. Since the signals of different wave modes overlap, we use vertical Fourier decomposition to extract the $n = 1$ component from the tropospheric vertical motion $W(z)$ following the formula (Stephan et al. 2016; AS20)

$$W(z) = \sum_{n=1}^{10} P_n \sin\frac{\pi n z}{D},$$

where P_n is the coefficient of each component and z is the height. Then just the $n = 1$ component is reconstructed when P_1 is significant at a 95% confidence level. We select two points close to the wave source ($X = 15$ and 30 km) to estimate the wave propagation speed and track it backward linearly to determine the wave generation time at the source, as higher-frequency waves are more evident near the source. According to Fig. 8, the $n = 1$ waves propagate at speeds of 35.7, 31.2, 27.8, 27.8, 25, and 25 m s^{-1}. Their generation time is then calculated by assuming a constant wave speed and

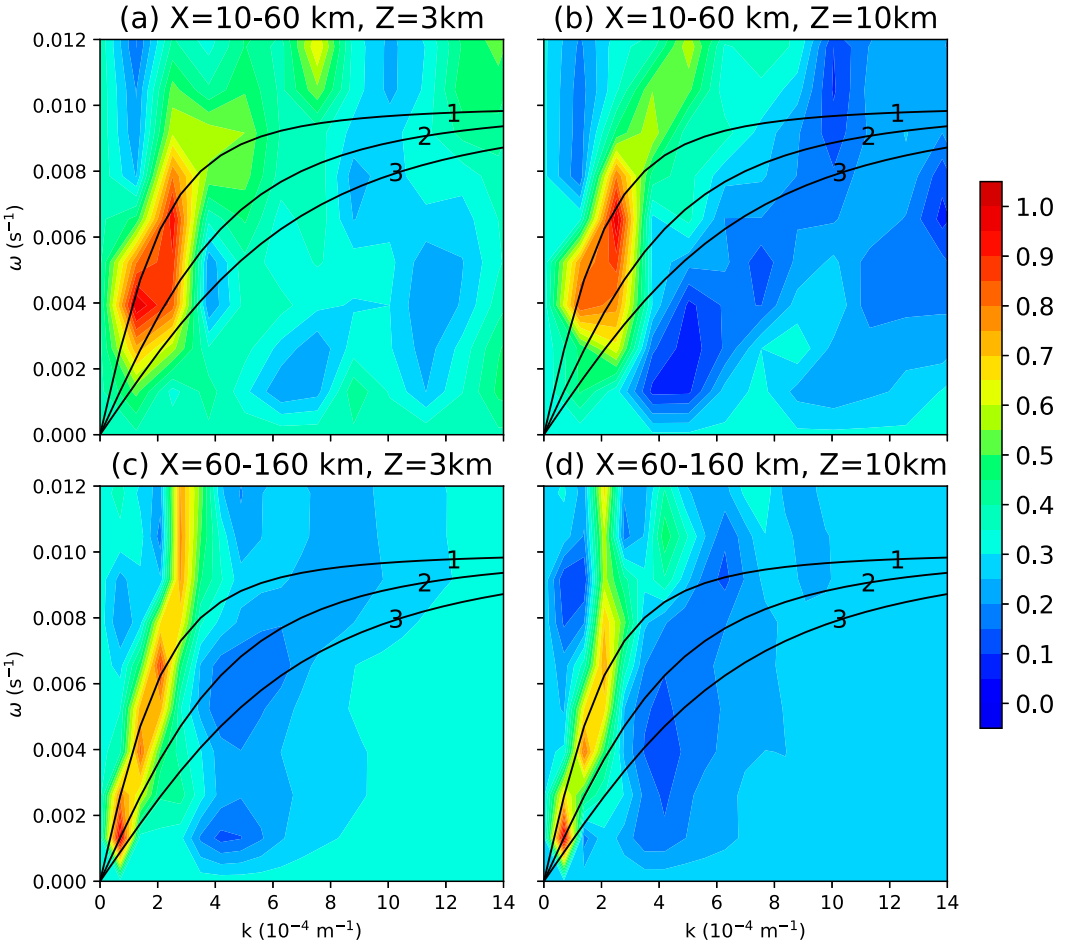

FIG. 7. Normalized two-dimensional (ω–k) power spectrum of vertical motions at (a),(c) Z = 3 km and (b),(d) Z = 10 km of two regions: (a),(b) X = 10–60 km (close to the source region) and (c),(d) X = 60–160 km (far from the source region) for MOIST experiment. Overlaid are curves of vertical wavelength of 24, 12, and 8 km (i.e., n = 1, 2, 3) calculated using nonhydrostatic dispersion relation, respectively.

interpolating wave motion back to X = 0 km (gray lines in Figs. 9 and 10).

Figure 9 depicts the vertically accumulated heat budget averaged in the convective region (i.e., over the central 10 km of the domain) at different layers. In Fig. 9a, the timing of n = 1 wave generation is found to best correlate with the local heating rate ($\partial\theta'/\partial t$), the variation in which is influenced by various convective processes. The vertical modes in each term of the heat budget are further analyzed using Fourier decomposition, which shows that the variation in the local heating rate corresponds well with that of its n = 1 component (Fig. 10a). When the n = 1 component of the local heating rate reaches its maximum (minimum) value, a downward (upward) branch of n = 1 wave is generated correspondingly. In previous studies (McAnelly et al. 1997; Stephan et al. 2016; AS20; Groff et al. 2021), such a generation of n = 1 waves is directly connected to the periodic development of latent heating. In the present study, a weak redevelopment of cloud (i.e., another peak of latent heating at 35 min, red line in Fig. 9a) is noticed and a downward branch of n = 1 wave should be expected accordingly. Instead, an upward branch (the second gray dashed line in Fig. 9) appears after 35 min, which is mainly forced by adiabatic cooling (blue lines in Fig. 9), while latent heating acts to decrease wave amplitude. In addition, vertical and horizontal advection terms contribute to wave generation and wave amplitude, especially at high levels (Fig. 9d). Note also that the amplitude of the first upward branch is larger than that of the first downward branch (Figs. 6a and 8a), but this is not the case in the next two couplets, which can be explained through their corresponding amplitude of the local heating rate (black line in Fig. 9a). While NPC91 explained the difference in wave amplitude by the upward energy escaping, our results provide another possibility.

In Fig. 10, the vertical distribution of each term in Fig. 9 (nonlinear advection is calculated as the sum of vertical and horizontal advection terms) is further exhibited. As the cloud develops, latent heat starts to release from low level and quickly extends to the whole troposphere and then lasts for about 10 min (Fig. 10b). The vertical distribution of latent heating features a maximum at the middle level of the

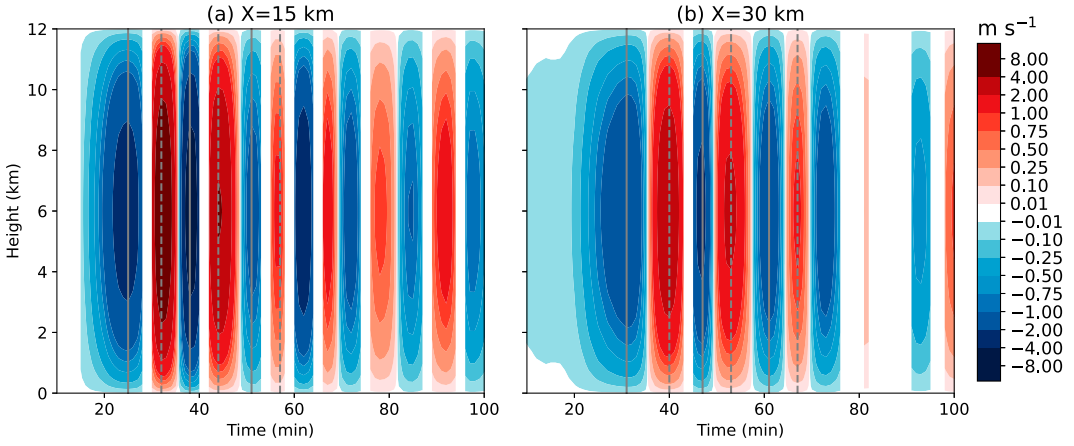

FIG. 8. Time–height diagram of reconstructed vertical motion (m s^{-1}) of $n = 1$ mode at (a) $X = 15$ km and (b) $X = 30$ km from the MOIST experiment. Only the coefficient that is significant at a 95% confidence level are shaded. Gray solid and dashed lines indicate the downward and upward motions of $n = 1$ wave couplets, respectively.

troposphere (~6 km). This feature is also confirmed by Fourier decomposition (black line in Fig. 10b), suggesting that latent heating is the primary contributor to the local heating rate responsible for initial $n = 1$ wave generation. Adiabatic cooling evolves quickly as a response to latent heating (Fig. 10d). Meanwhile, increased vertical motion inside convection (Fig. 4) enhances nonlinear advection (mainly vertical advection, shown in Figs. 9 and 10c), of which the amplitude is comparable to that of latent heating (Fig. 9a). The amplitude of nonlinear advection is roughly twice as intense as latent heating at high levels (Fig. 9d). The opposite contribution of vertical advection occurs in the upper and lower troposphere, and the contribution of horizontal advection is negligible at low levels (Fig. 9). Furthermore, the presence of both $n = 1$ and $n = 2$ components in the vertical profile of nonlinear advection, as depicted in Fig. 10c, suggests that nonlinear advection may play a role in generating both $n = 1$ and $n = 2$ waves.

Because of the dominant role of latent heating, the timing of the downward branch in the first wave generation (19 min) is near the time when latent heating reaches a maximum (Figs. 9a and 10b). However, the effects of nonlinear advection and adiabatic heating/cooling cannot be neglected. After 20 min, latent heating and nonlinear advection start to weaken, and the adiabatic cooling becomes strongest (Fig. 9a). Consequently, the generation of the first $n = 1$ upward branch is attributed to the combination of latent heating, nonlinear advection, and adiabatic cooling. While latent heating remains small between 25 and 30 min, the second downward branch starts to emanate from the source region, and the local heating rate is mainly controlled by adiabatic heating at that time (Fig. 10d). This means the second downward branch is not a direct result of reinvigorated latent heating forcing but instead a compensating subsidence to the decrease in mass flux in the source region.

At approximately 30 min, latent heating strengthens again but with a reduction in both magnitude and vertical range (Figs. 9 and 10b). Nevertheless, latent heating cannot overcome the effect of adiabatic cooling at this time since the updraft is still strong. Hence, the second upward branch is generated at 35 min. For the third wave couplets, since evaporation-induced latent cooling and associated adiabatic heating are almost in balance with each other ($\partial\theta'/\partial t \sim 0$; Fig. 9), waves are generated at 41 and 47 min with small amplitudes. As emphasized by Wang et al. (2018), one more interesting point is that the evolution of nonlinear advection roughly follows latent heat release. Once latent heat is released, nonlinear advection strengthens (Figs. 10b,c). The time scale of nonlinear advection is about half that of latent heating (Fig. 10c), which suggests that waves forced by nonlinear advection may have a relatively higher frequency. This is in line with the expectation, as the spectrum displays two prominent power centers, one corresponding to waves with a higher frequency of 6×10^{-3} s^{-1} and another with a frequency of 4×10^{-3} s^{-1} (Fig. 7).

The imbalance between latent heating and adiabatic heating/cooling indicates the important role of the *deep heating* mechanism in explaining wave generation, but strong nonlinear advection should also be taken into account. This is because the imbalance initially induced by latent heating is found to be further enhanced by nonlinear advection. The analysis above shows that these two forcings should work jointly to enable wave generation, but their relative roles are uncertain due to the complexity of moist convection (e.g., Wei and Zhang 2014) and coupled wave–convection relationship (e.g., Du and Zhang 2019; Ruppert et al. 2022). As seen in Fig. 3c, the formation of new clouds might also trigger gravity waves and exert a strong influence on the amplitude of preexisting waves, which complicates the processes. Thus, it is necessary to employ dry experiments with controllable artificial latent heating to obtain a better understanding of wave generation.

4. Generation of gravity wave couplets by artificial latent heating

In this section, we further demonstrate the wave generating processes by conducting an idealized dry experiment with

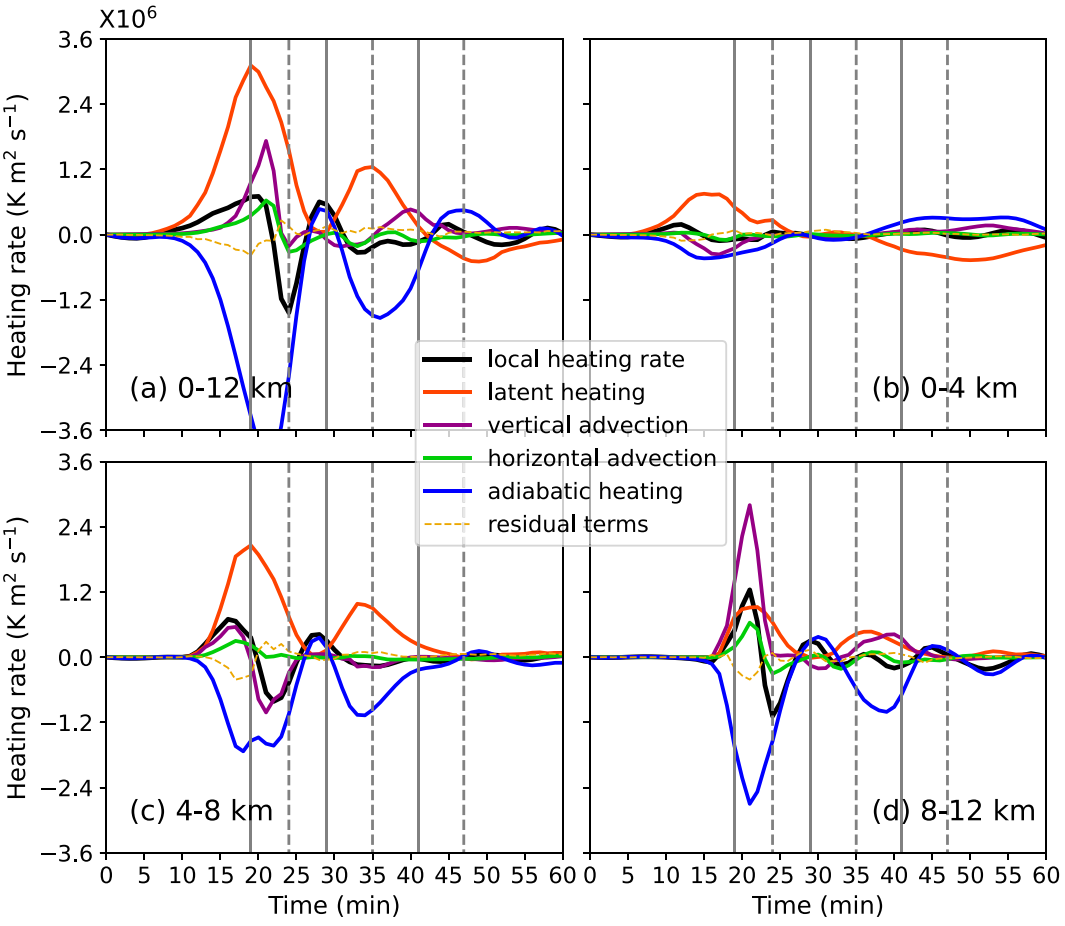

FIG. 9. Vertically accumulated heat budget for (a) the whole troposphere, (b) low level, (c) middle level, and (d) high level of troposphere over the horizontal $X = -5$ to 5 km region. Gray solid and dashed lines represent the generation time of downward and upward motions of $n = 1$ gravity waves, respectively.

prescribed artificial latent heating. As described in sections 2b and 2c, the simulation was forced by a diabatic heat source designed to imitate latent heating in the MOIST experiment (see Table 1). Different from previous theoretical (NPC91; McAnelly et al. 1997) and modeling (e.g., Lane and Zhang 2011) studies using pulse or periodic heating sources, the temporal form is set to conform the Gaussian distribution (red solid line in Fig. 3) to accurately match the actual variation in latent heating (Figs. 9a and 10b).

Figure 11 shows a Hovmöller diagram of the vertical velocity at two different levels of the troposphere in the CTRL experiment. Similar to the results in the MOIST experiment (Fig. 5), the first two $n = 1$ wave couplets are observed (denoted by black lines in Fig. 11) while subsequent $n = 1$ waves are generated with smaller amplitudes. Additionally, when latent heating is turned off (after 25 min), $n = 2$ waves are also produced and propagate outward with a slower wave speed (~18 m s^{-1}, green lines in Fig. 11b). As shown in Fig. 11b, later generated $n = 1$ waves will superimpose on earlier generated higher-order waves because $n = 1$ waves have a faster speed.

The dispersion and polarization relations of waves propagating in the troposphere are first examined in Fig. 12. It is evident that both waves near and far from the source are primarily hydrostatic and of $n = 1$ mode (Figs. 12a–d). However, although the dispersion relation of higher-frequency waves (the power peak at 8.2×10^{-3} s^{-1}) does not match the $n = 1$ curve neatly, they still share almost the same horizontal phase speed with lower-frequency waves (the power peak at 4×10^{-3} s^{-1}), indicating the possible role of wave ducting (Figs. 12a–d). A possible mechanism is the inversion of the temperature gradient at the tropopause, which might contribute to the formation of deep tropospheric wave couplets (Lindzen and Tung 1976; NPC91). Figure 12e also shows that the largest downward vertical velocities are located a quarter wavelength downstream from where the eastward horizontal velocities are largest at low levels. Additionally, these nearly horizontally propagating waves carry little net vertical momentum flux (Fig. 12f). Nonetheless, the presence of higher-frequency waves with a vertical component contributes to a substantial concentration of net momentum flux features a large value near the tropopause (~12 km). The wave propagation in the lower stratosphere results in upward momentum flux transmission (centered at ~15 km),

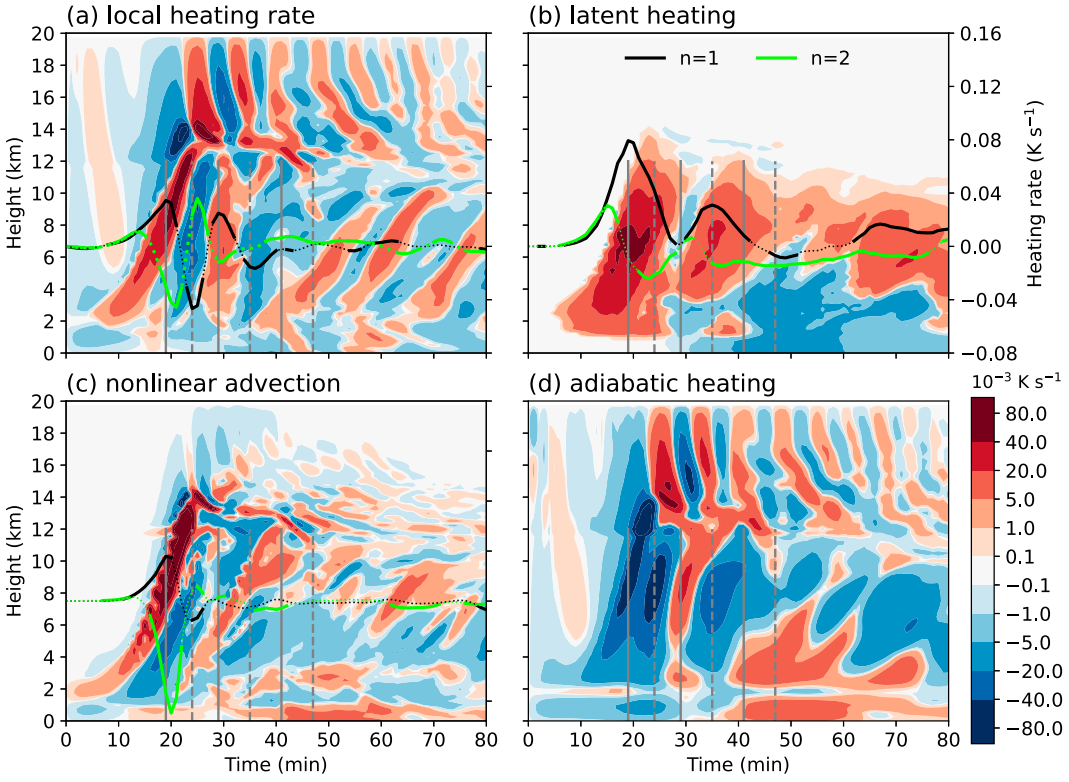

FIG. 10. Temporal evolution of the horizontally averaged ($X = -5$ to 5 km) (a) local heating rate (K s^{-1}), (b) latent heating (K s^{-1}), (c) nonlinear advection (K s^{-1}), and (d) adiabatic heating (K s^{-1}). Gray solid and dashed lines represent the generation time of downward and upward motions of $n = 1$ gravity waves, respectively. Black and green lines overlaid in (a)–(c) are the $n = 1$ and $n = 2$ coefficients derived from vertical Fourier decomposition of each term, respectively, and only shown in solid if the coefficient is statistically significant, with the right axis in (a)–(c) corresponding to their values.

although it is largely depressed by Rayleigh damping near the top of the model domain (Fig. 12f). Since waves propagate at a constant speed if the background condition does not vary, the accurate $n = 1$ wave speeds and the timing of their generation can be estimated from two selected points far away from the source ($X = 50$ and 100 km) that exhibit evident $n = 1$ like structures (Fig. 13). According to Fig. 13, the horizontal phase speeds of these $n = 1$ waves are 36–44 m s^{-1}.

Figure 14 depicts the generation and outward propagation of gravity waves. As latent heating reaches a maximum at 15 min (Fig. 3), the first downward branch reaches its maximum amplitude and starts to propagate at a speed of approximately 40 m s^{-1} (Figs. 14a,b). The strongest downward vertical motion occurs in the middle level (~6 km), corresponding well with the vertical distribution of the heating source. Its counterpart (the first upward branch) is soon generated with a larger amplitude (Fig. 14b). Later, owing to the shutdown of latent heat supply, the second $n = 1$ wave couplet is triggered with a smaller wave amplitude (Fig. 14c). Evidence of higher-order wave signals (e.g., a $n = 2$ wave in the purple box in Fig. 14b) can be seen close to the source (Fig. 14b). The vertical structures of $n = 1$ waves become more apparent as they quickly propagate away from the source (Figs. 14c,d).

The heat budget analysis can show in detail that convective processes favor more generation of $n = 1$ waves. Figure 15 shows the vertical distribution evolution of each term in the heat budget of the CTRL experiment. The results before 30 min are similar to those in the MOIST experiment (Fig. 10), which makes our subsequent analysis more reliable.

The timing of wave couplet generation was obtained by tracing backward linearly to the source region according to their phase speed (Fig. 13). The downward branches for two $n = 1$ wave couplets both correspond to positive local heating rates (Fig. 15a), which is consistent with what we obtained in section 3c (Fig. 9). What we observed in the vertical motion field should be a combination of wave modes. The generated $n = 1$ and $n = 2$ waves are a natural response to the $n = 1$ and $n = 2$ components of the local heating rate (Fig. 15a). Since $n = 1$ wave couplets propagate much faster than higher-order waves and a relatively small proportion of higher-order wave components is contained in local heating rate profile, wave couplets in the far field are mainly $n = 1$ mode. Therefore, the question raised here is why the local heating rate profile could still contain a large $n = 1$ component when latent heating is weak.

Deeper insight is provided on how the temporal variation and vertical distribution of the local heating rate is determined.

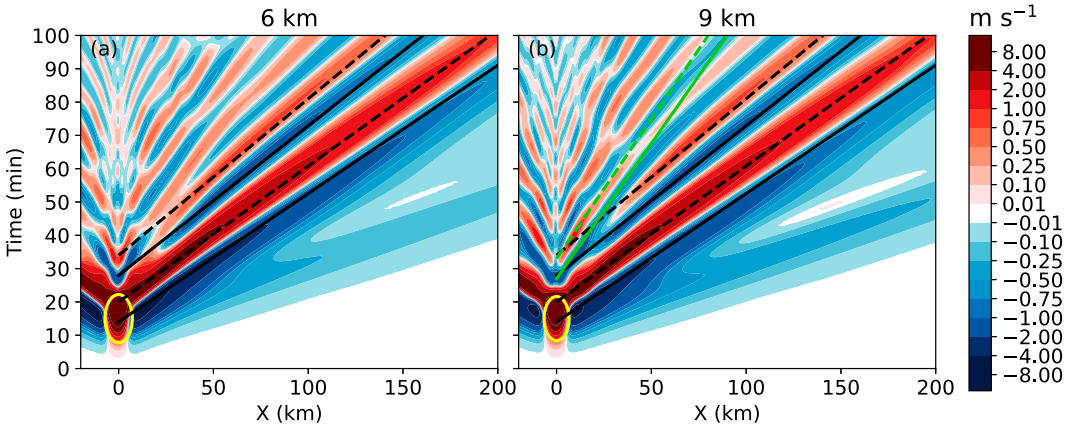

FIG. 11. Hovmöller diagram of vertical motion (m s^{-1}) at (a) 6 and (b) 9 km AGL from the CTRL experiment. Yellow contours indicate the latent heating (0.01 K s^{-1}) at each level. Black solid and dashed lines indicate the downward and upward motions of $n = 1$ wave couplets, with green solid and dashed lines in (b) indicating possible $n = 2$ waves with downward motion and upward motion at high levels.

As shown in Figs. 15a and 15c, adiabatic heating/cooling is found to be the main contributor to the local heating rate after around 25 min. Therefore, a question arises why the adiabatic heating/cooling still produces such strong oscillations even after the latent heating is turned off. Strong nonlinear advection is suggested as a possible cause. The wave frequency spectrum (Figs. 12a–d) shows two peaks, one at 4×10^{-3} s^{-1}, corresponding to a period of ~26 min close to that of latent heating (~25 min, Fig. 15d), and the other at approximately twice that (8.2×10^{-3} s^{-1}, period of ~13 min). This implies that nonlinear advection also plays a significant role in the oscillation of the local heating rate, with its shorter period of ~15 min (Fig. 15b).

As analyzed in the last section, nonlinear advection is nonnegligible in the MOIST run. In the CTRL run, the effect of the nonlinear advection on wave amplitude is more evident because the artificial latent heat release does not start from low levels as in MOIST. As shown in Fig. 15b, the magnitude of nonlinear advection is larger in the upper troposphere than in the lower troposphere and reaches a peak at the top of the heating (or tropopause, Fig. 15b). This is because of upward heat transfer, i.e., upward motion associated with latent heating results in a larger potential temperature perturbation to the upper level through vertical advection (Figs. 15e,f). Therefore, the magnitude of nonlinear advection is strongest after latent heating reaches its maximum and cannot be neglected in the generation of $n = 1$ wave couplets. We conclude that understanding wave generation requires considering both the *deep heating* mechanism and nonlinear advection. The balance effect of adiabatic heating/cooling is partially offset by nonlinear advection (evident before 25 min in Figs. 15b,c), resulting in a more persistent imbalance in the upper troposphere (e.g., $\partial\theta'/\partial t \neq 0$, purple boxes in Fig. 15) and a larger $n = 1$ component in the local heating rate profile (Fig. 15a), which enables more $n = 1$ wave couplets to be emitted. Despite the prescribed latent heating being purely $n = 1$ mode, nonlinear advection also contributes greatly to the generation of higher-order waves (e.g., $n = 2$ waves in Fig. 11), as seen from its vertical profile (Fig. 15b).

5. Sensitivity experiments

Based on the analysis of the two sections above, we found that the temporal variation in the local heating rate determines the timing of wave generation in the troposphere, and we examined the different roles of latent heating and nonlinear advection in initiating gravity waves. To further validate these findings and explicitly clarify their roles, we conducted the following sensitivity experiments by modulating artificial latent heating parameters.

a. Latent heating with different temporal variations

Latent heating in realistic moist convection consists of an extensive range of frequencies, but in many linear wave theories, heat forcing is considered to be relatively constant (e.g., NPC91; Han and Baik 2012) or transient (e.g., Han and Baik 2009). Convectively generated gravity waves are mostly observed with periods between 10 and 100 min (Alexander et al. 1995; Beres et al. 2004). How various temporal variations in latent heating impose effects on wave generation is an unclear question. Here we examine three temporal forms of artificial latent heating. The time of hydrostatic wave generation is determined using the same method as in CTRL by linearly tracking backward at $X = 50$ and $X = 100$ km in time–height diagrams.

In the Steady_heat experiment (Fig. 16b), the latent heat release is specified to reach a maximum rapidly (about 5 min), then be maintained for about 40 min, and finally weakens rapidly (about 5 min). As shown in Fig. 16b, the wave response is quite different from the result in the CTRL run (Fig. 16a). Approximately two $n = 1$ wave couplets are excited when latent heating is nearly unchanged (between 15 and 40 min), which further proves that $n = 1$ wave signals cannot simply correspond to the variation in latent heating. Instead, the timing of wave generation is associated with the variation

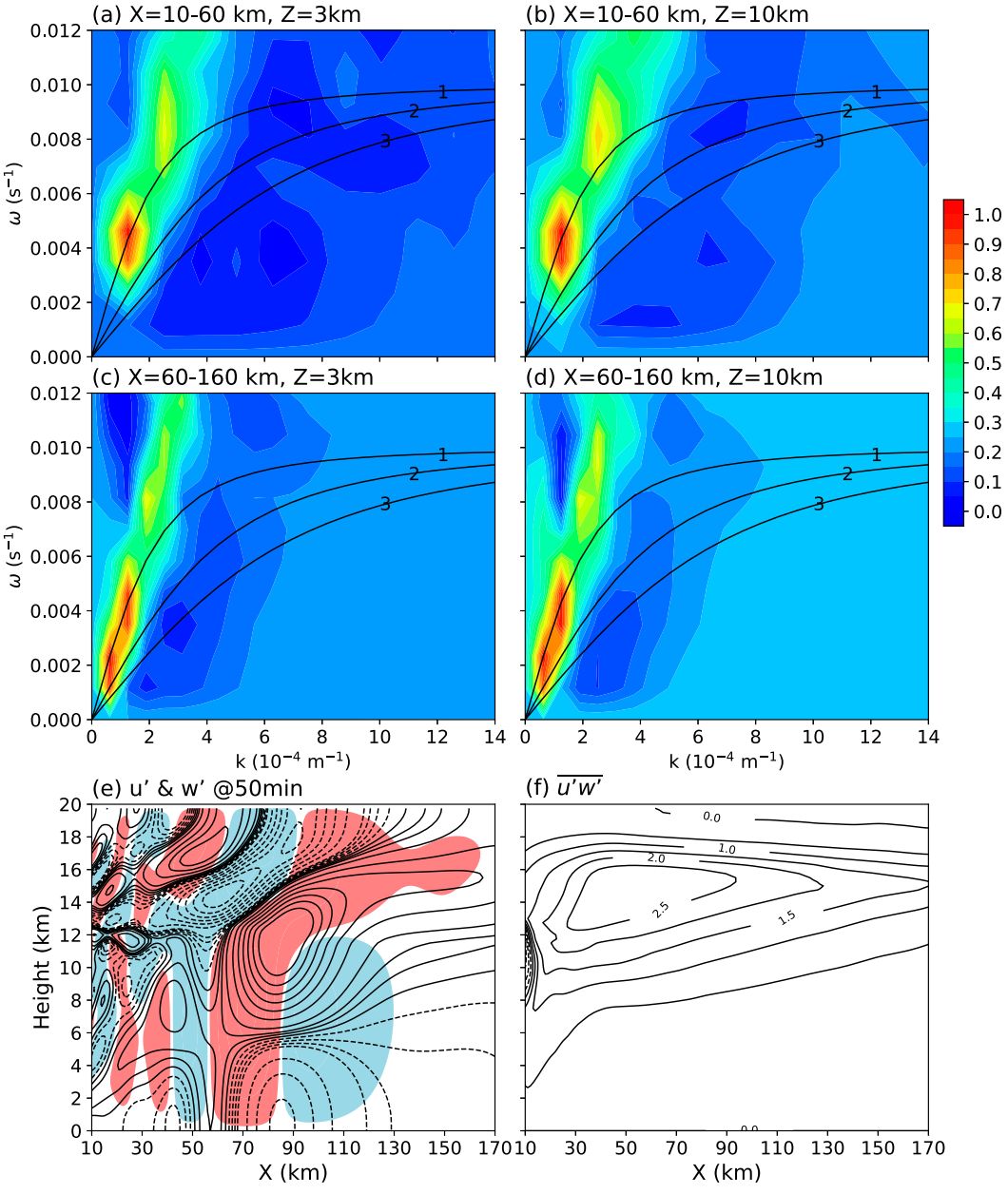

FIG. 12. (a)–(d) As in Fig. 7, but for CTRL experiment. (e) Horizontal velocity perturbation (contoured; m s^{-1}) and vertical motion (shaded; m s^{-1}) at 50 min for CTRL experiment, with blue and red shading delineating downward and upward motions, respectively. Contour intervals are 0.5 m s^{-1} for absolute values less than 3 m s^{-1} and contour intervals are 3 m s^{-1} for absolute values larger than 3 m s^{-1}. (f) Distribution for net momentum flux (m^2 s^{-2}) after integration of 2 h. Contour interval is 0.5 m^2 s^{-2} with negative values dashed.

in the local heating rate in the source region, as shown in Fig. 17a. Persistent latent heating helps maintain the strength of the main updraft in the source region. But due to the opposing force of adiabatic cooling, the main updraft undergoes enhancement and weakening (Fig. 17j), which is clearly linked to the variation in nonlinear advection and adiabatic heating (Figs. 17g,j), thus leading to the extreme imbalance state ($|\partial\theta'/\partial t|$ is large, 0–40 min, Fig. 17a) and periodic wave generation. When latent heating, adiabatic cooling, and nonlinear advection reach a balanced state (40–50 min in Figs. 16b and 17a), almost no wave is generated (or too weak to be seen). Additionally, due to the similar contribution of nonlinear advection with adiabatic cooling in the lower troposphere, it is found that the lower troposphere can recover much faster before the shutdown of heating (Fig. 17a).

In the Reinforce_heat run, multiple wave couplets are triggered with the redevelopment of artificial latent heating (Fig. 16c), which is similar to the MOIST experiment. In this

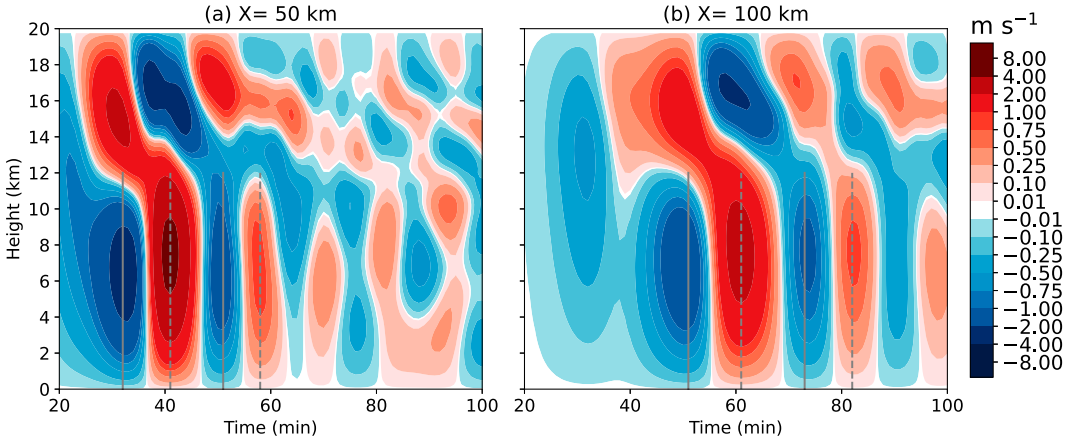

FIG. 13. Time–height diagram of vertical motions (m s^{-1}) at (a) $X = 50$ km and (b) $X = 100$ km from the CTRL experiment. Gray solid and dashed lines indicate the downward and upward motions of $n = 1$ wave couplets, respectively.

case, the timing of the second wave generation (29 min in Fig. 17b) is slightly earlier than the timing when latent heating reaches a maximum at 30 min. This is because the nonlinear advection induced by the first latent heat release is not fully balanced when the latent heating is enhanced again (Fig. 17h). And the more gradual onset of the second latent heating, as well as the slower strengthening of nonlinear advection, may also contribute to the local heating rate to peak earlier. Compared with Fig. 16a, the first wave couplets in the two experiments are almost the same but the second wave couplets show some differences between the two experiments. The signal of the second $n = 1$ wave couplet is noticed only after wave propagating for a period in CTRL while in the Reinforce_heat run, the

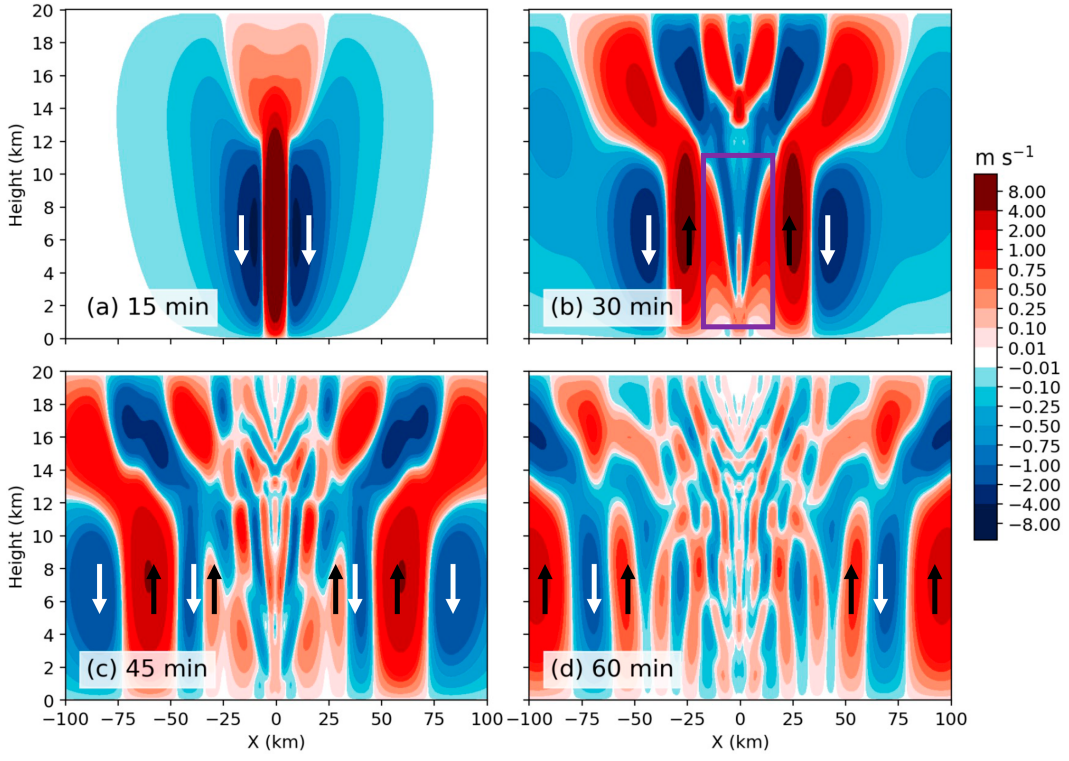

FIG. 14. Vertical cross sections of vertical motion (shaded; m s^{-1}) for the CTRL experiment at (a) 15, (b) 30, (c) 45, and (d) 60 min. White and black arrows denote the downdraft and updraft of the first two wave couplets, respectively. Purple box in (b) shows the early signal of the second downward branch of $n = 1$ associated with an $n = 2$ wave.

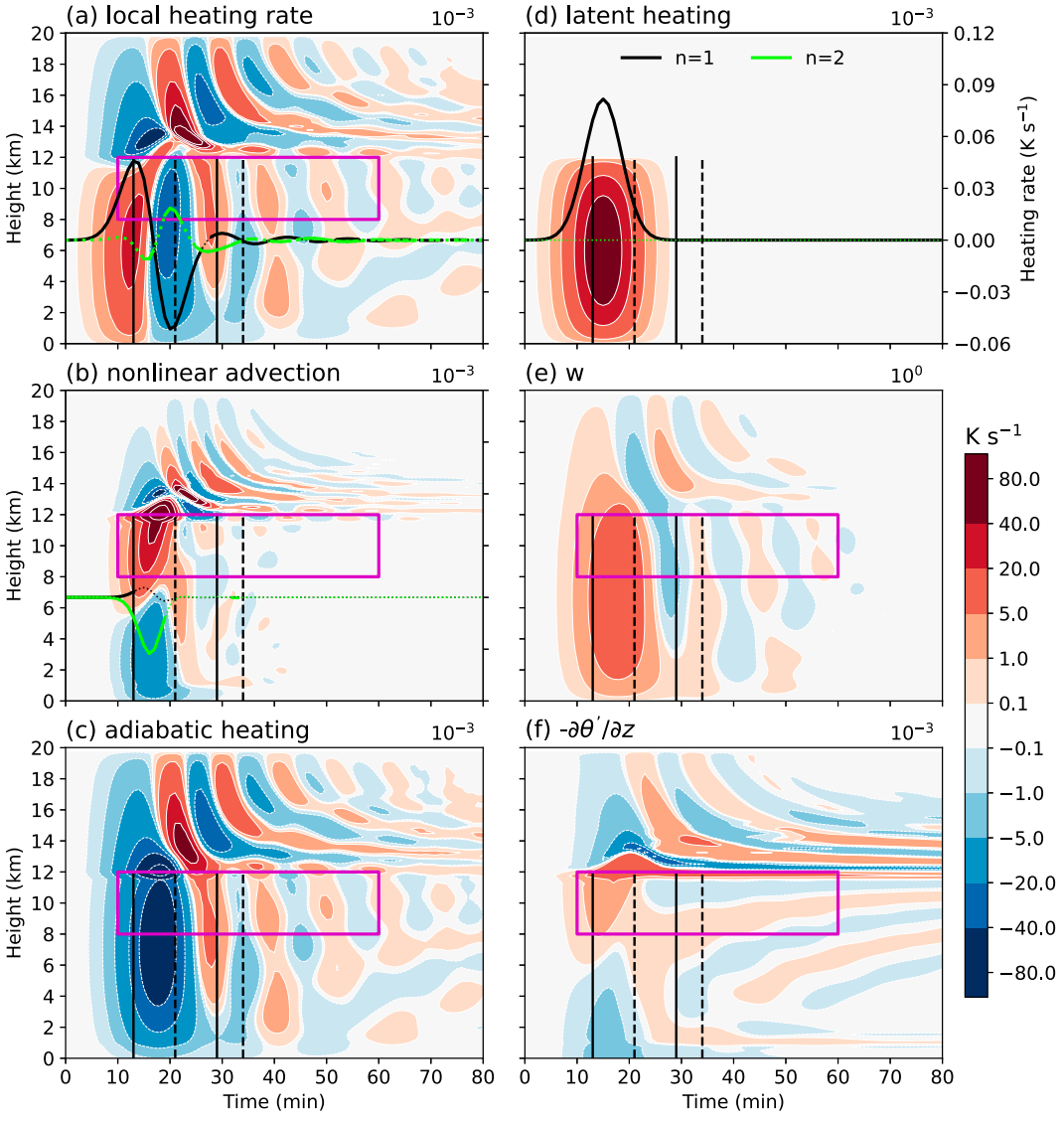

FIG. 15. Temporal evolution of the horizontally averaged ($X = -5$ to 5 km) (a) local heating rate (K s^{-1}), (b) nonlinear advection (K s^{-1}), (c) adiabatic heating (K s^{-1}), (d) latent heating (K s^{-1}), (e) vertical motion (w; m s^{-1}), and (f) negative vertical gradient of potential temperature perturbation ($-\partial\theta'/\partial z$; K m^{-1}) in the CTRL experiment. For comparisons, values in each subplot are scaled by their magnitude (listed in the right-upper corner of each panel). Purple boxes represent areas of the upper atmosphere. Black solid and dashed lines represent the time when the amplitudes of downward and upward motions of $n = 1$ gravity waves reach maximum, respectively. Black and green lines overlaid in (a)–(c) are the $n = 1$ and $n = 2$ coefficients derived from vertical Fourier decomposition of each term, respectively, and only shown in solid if the coefficient is statistically significant, with the right axis in (a)–(c) corresponding to their values.

signal is still significant in the vicinity of the source. This can be explained by the extra deep latent heating (Fig. 17e), although its strength is smaller. Consequently, the wave amplitude of the second wave couplet is also smaller than that of the first $n = 1$ wave couplet. Note that the smaller amplitude is determined by the corresponding weaker adiabatic cooling and smaller local heating rate (Figs. 17b,k). In general, both the results in Steady_heat and Reinforce_heat show that wave generation is the response to the variation in local heating rate and highlight the importance of nonlinear advection.

In the Slow_heat run, the timing of the first downward motion branch's generation (at 27 min, Figs. 16d and 17c) is much earlier than the peak time of latent heating (at 35 min, Fig. 3). The reason is that the enhancement of latent heating in the Slow_heat run is much slower, but the strength of vertical motion is comparable to that in the Reinforce_run, so adiabatic cooling can offset latent heating in an earlier time (Fig. 17l).

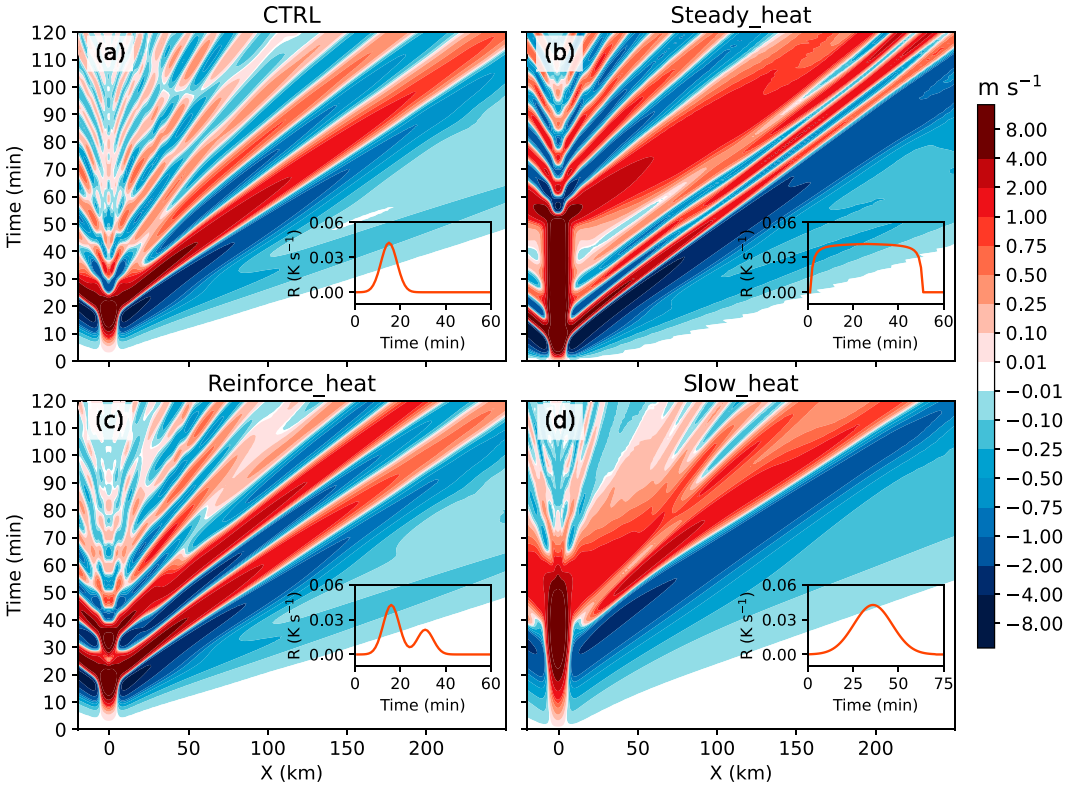

FIG. 16. Hovmöller diagram of vertical motions (m s^{-1}) at 6 km AGL from the (a) CTRL, (b) Steady_heat, (c) Reinforce_heat, and (d) Slow_heat experiments. The corresponding temporal form of artificial latent heating in each experiment is embedded in each subplot with x axis denoting time (min) and y axis denoting heating rate R (K s^{-1}).

Also, the nonlinear advection is weaker, compared with the other two experiments (green boxes in Figs. 17g–i), which could result in a faster recovery of the atmosphere and relatively weaker wave couplet signals (Fig. 16d). This phenomenon will be further explored in the next sensitivity experiment.

b. *Degree of system nonlinearity*

Previous studies have noted how nonlinear effects may influence wave dynamics (Lane et al. 2001; Song et al. 2003; Chun et al. 2008; Han and Baik 2012) and convection structure (Pandya and Durran 1996). By changing the nonlinearity factor in a nondimensional model, Han and Baik (2012) found that nonlinear effects could influence wave generation. As we analyzed in sections 3 and 4, strong latent heating is accompanied by strong nonlinear advection, which suggests a large degree of system nonlinearity. Different from Han and Baik (2012), herein we measure the degree of system nonlinearity by comparing the magnitude of latent heating and nonlinear advection. The Q_linear run forced by one percent of the strength of artificial latent heating in CTRL is performed to examine the role of nonlinear advection in wave generation (Pandya and Alexander 1999; Song et al. 2003). As shown in Fig. 18g, the Q_linear run is characterized by weak nonlinear advection, and thus can be considered as a quasi-linear experiment.

Figure 19 shows the comparison of wave responses between the CTRL and Q_linear experiments. To make a reasonable comparison, results in the Q_linear run are multiplied by a coefficient of 100. Although waves in these two experiments seem to be generated roughly at the same time (Figs. 18a,e), as system nonlinearity decreases, multiple wave couplets' signals are less evident in the Q_linear run compared with the CTRL run (e.g., the second $n = 1$ wave couplet in Fig. 19). In contrast to CTRL, spectrum analysis also shows that higher-frequency $n = 1$ waves have little energy and be less important in the Q_linear experiment (figure not shown). By comparing Figs. 18c and 18g, it is found that nonlinear advection is almost zero in Q_linear, while its magnitude is considerable in CTRL. Hence, adiabatic cooling can offset latent heating effect to a greater extent when latent heating is weak (Figs. 18d,h), and fewer $n = 1$ components are found in the vertical profile of the local heating rate after heating is turned off because of the faster recovery (black boxes in Figs. 18a,e). This further implies that nonlinear advection can contribute significantly to wave generation in actual convection.

However, it is important to note that in the Q_linear experiment (Fig. 18b), besides the evident $n = 1$ wave couplet, additional $n = 2$ and $n = 3$ waves (only one branch of them) are generated, which is unexpected considering the perfect $n = 1$ shape of the heating profile (Fig. 18f). By performing vertical Fourier decomposition of the source region, it is revealed that these higher-order waves originate from the adiabatic heating term (Fig. 20). This

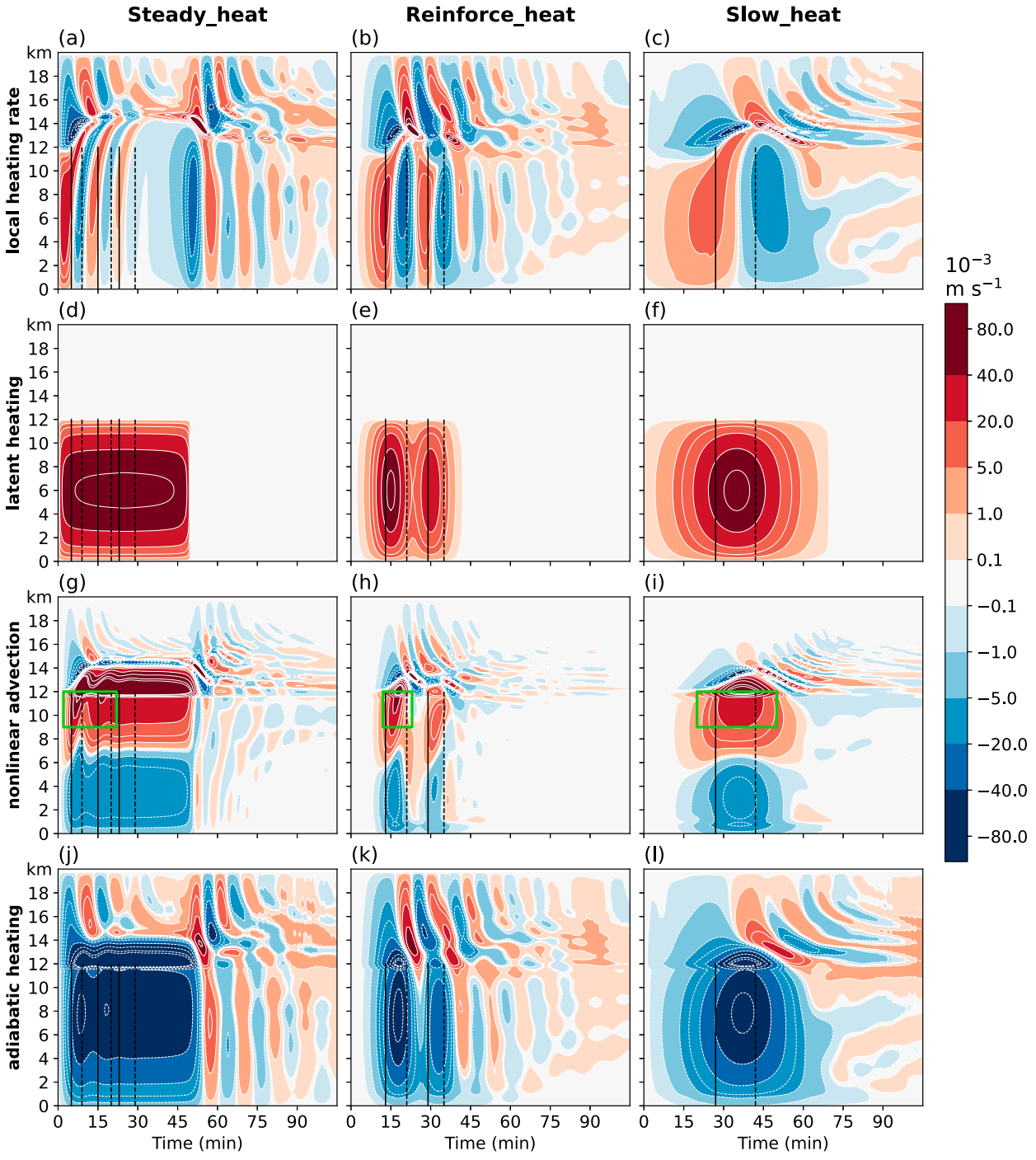

FIG. 17. Temporal evolution of the horizontally averaged ($X = -5$ to 5 km) (a)–(c) local heating rate (K s^{-1}), (d)–(f) latent heating (K s^{-1}), (g)–(i) nonlinear advection (K s^{-1}), and (j)–(l) adiabatic heating (K s^{-1}) for the (a),(d),(g),(j) Steady_heat, (b),(e),(h),(k) Reinforce_heat, and (c),(f),(i),(l) Slow_heat experiment. Black solid and dashed lines represent the time when the amplitudes of downward and upward motions of $n = 1$ waves reach maximum, respectively. Green boxes in (g)–(i) delineate the maximum of nonlinear advection in three experiments.

discrepancy might be attributed to the vertically heterogeneous distribution of buoyancy frequency (larger in the upper troposphere, Fig. 2), which has been assumed constant in our experiments and many previous theoretical studies (e.g., NPC91; Beres 2004). Given the sensitivity of vertical motion response to buoyancy frequency, especially when the strength of latent heating is relatively weak, higher-order waves might be excited as a result. However,

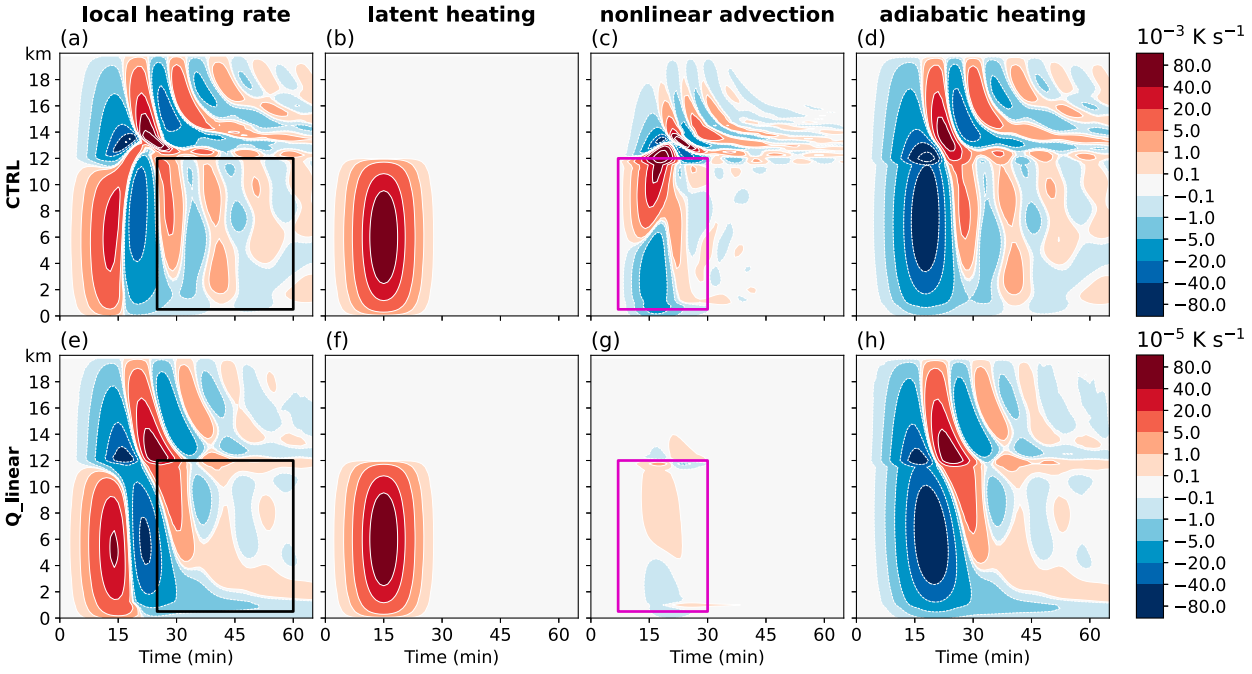

FIG. 18. Temporal evolution of the horizontally averaged ($X = -5$ to 5 km) (a),(e) local heating rate, (b),(f) latent heating, (c),(g) nonlinear advection, and (d),(h) adiabatic heating for (a)–(d) CTRL and (e)–(h) Q_linear experiments. (a)–(d) for CTRL are from Fig. 15. Purple boxes in (c) and (g) represent nonlinear advection in the troposphere, and black boxes in (a) and (e) show the variation in the local heating rate in the troposphere when latent heating is turned off.

further detailed analysis is necessary in further studies to fully understand this phenomenon.

6. Conclusions and discussion

The present study employs Cloud Model 1 to investigate the mechanisms behind the generation of gravity waves by convection, which consist of multiple deep tropospheric downdraft–updraft couplets. The potential temperature equation in the model was modified to reflect variations in latent heating when moist processes were turned off in dry simulations. The key findings are as follows:

1) Multiple significant $n = 1$ wave couplets with wave fronts that cover the entire depth of the troposphere are generated during the evolution of a convective cloud, as well as in dry experiments with prescribed latent heating.

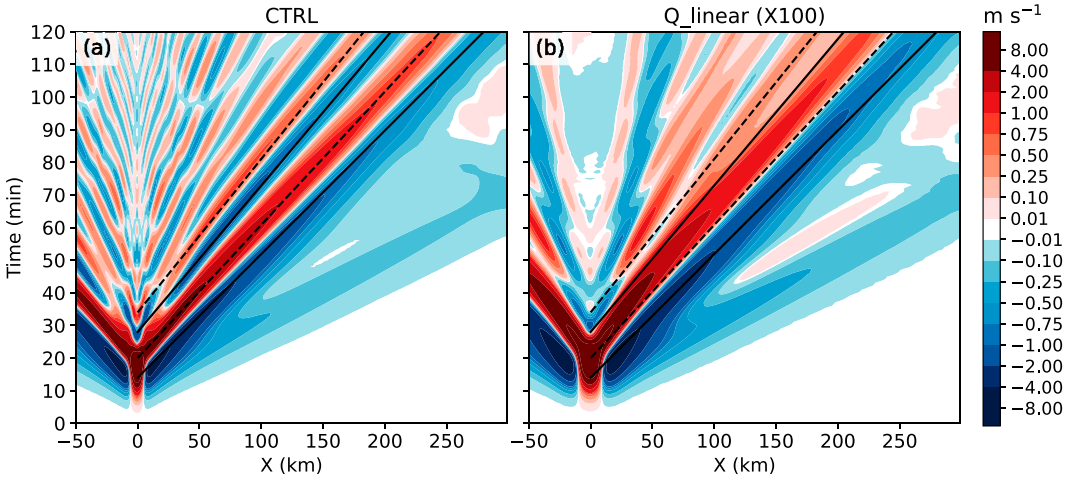

FIG. 19. Hovmöller diagram of vertical motion (m s^{-1}) at 6 km AGL from (a) CTRL and (b) Q_linear experiments. Vertical motion in (b) is multiplied by a coefficient of 100 derived from the heating rate ratio between Q_linear and CTRL. Black solid and dashed lines are downward and upward branches of $n = 1$ waves in CTRL, respectively.

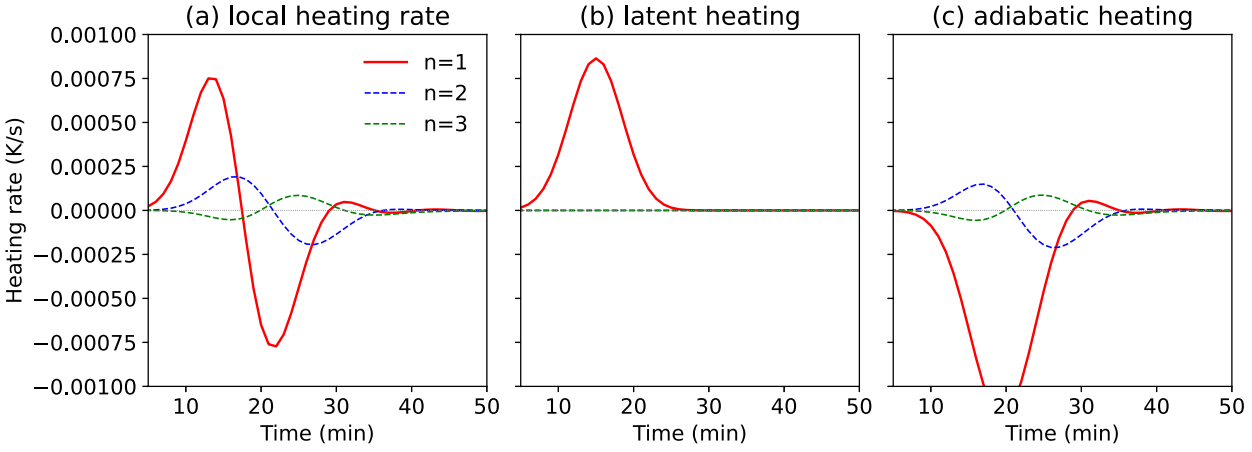

FIG. 20. Vertical Fourier decomposition of horizontally averaged ($X = -5$ to 5 km) (a) local heating rate, (b) latent heating, and (c) adiabatic heating for Q_linear experiment.

2) These waves exhibit a substantial horizontal component of group velocity and consist primarily of hydrostatic waves. They propagate away from the convective cloud at a high speed (~37 m s^{-1}), greatly impacting the cloud environment by changing the MUCAPE field.
3) The timing of wave generation is closely tied to variation in the local heating rate, which is primarily controlled by the imbalances among latent heating, nonlinear advection, and adiabatic heating/cooling. The magnitude of the local heating rate also closely corresponds to the amplitude of $n = 1$ wave couplets.
4) Heat budget analysis reveals that the generation of the first wave couplet is mainly driven by strong latent heating, with adiabatic heating/cooling immediately balancing it. The upward heat transfer from the strong updraft in the source region, however, greatly enhances nonlinear advection. As a result, persistent buoyancy oscillation over the entire troposphere could persist for a longer time due to the opposite contribution of nonlinear advection and adiabatic heating/cooling at high levels, leading to the generation of successive $n = 1$ wave couplets and higher-order waves (e.g., $n = 2$ waves).

This study differs from previous studies that mainly linked wave generation to variations in latent heating (Mapes 1993; McAnelly et al. 1997; AS20; Groff et al. 2021), as it highlights the importance of nonlinear advection in wave generation as well. Nonlinear advection, which has been shown to be closely related to latent heating (Lane and Reeder 2001; Song et al. 2003; Wang et al. 2018), is found to interact with latent heating and create a more persistent state of imbalance. The local heating rate serves as a good indicator of the degree of imbalance, and also explains the discrepancies in wave amplitude observed in previous studies (NPC91; AS20; Groff et al. 2021).

The simulations in this study have a limitation in that they were performed in a 2D framework with a relatively coarse horizontal grid spacing. Sensitivity simulations (2D with 250 m in the horizontal; 3D with the same resolution) were conducted to examine this limitation. The dry experiment showed almost no change with a finer resolution, but moist convection was sensitive to the grid spacing as noted in previous studies (e.g., Bryan et al. 2003; Varble et al. 2020). Although latent heating and horizontal advection became larger due to a finer description of convection, so did adiabatic heating/cooling, the correlation between wave generation and local heating rate remained strong. The main conclusion of the study still holds in 3D simulations, although the amplitude of $n = 1$ waves was relatively smaller, which is expected as more wave energy is attenuated in a three-dimensional space. Additionally, long-lived convections often develop and propagate perpendicular to the background wind (e.g., Rotunno et al. 1988), suggesting that waves will have the most power in that direction (Beres 2004; Stephan et al. 2016). While a 2D analysis might be sufficient, it would be interesting to further explore our conclusions in a more realistic atmosphere.

Moreover, future studies should focus on the evolution of local heating rate in complex convective processes other than short-lived convection in this study. Will the role of the two forcings be the same in long-lived mesoscale convective systems? How will wave–convection interaction affects the generation of wave couplets? To what extent can the modification of the cloud environment by these waves impose influence on the evolution of convection, especially for higher-frequency waves if there exists a trapping mechanism? These are important issues that need to be addressed in future studies so that a better understanding of the coupled wave–convection relationship can be promoted.

Acknowledgments. We express thanks to Dr. Kim Young-Ha for constructive discussions, Dr. Rebecca Adams-Selin and Dr. Claudia Christine Stephan for kind technological support on code writing, and Prof. George Bryan for making CM1 available. This study was supported by the National Natural Science Foundation of China (Grants 42122033, 42075006, 42075005, and 42375003), the Guangdong Major Project of Basic and Applied Basic Research (2020B0301030004), the Key Innovation Team of China Meteorological Administration (CMA2023ZD08), Guangdong Province Key Laboratory for Climate Change and Natural Disaster Studies (2020B1212060025),

and the Innovation Group Project of Southern Marine Science and Engineering Guangdong Laboratory (Zhuhai) (311021001). The authors are also immensely grateful to the editor (Dr. Anne Smith), Dr. Rebecca Adams-Selin, and two anonymous reviewers for taking the time to review our paper and provide comprehensive comments.

Data availability statement. All simulation data and related codes are archived and available via request.

REFERENCES

Adams-Selin, R. D., 2020: Impact of convectively generated low-frequency gravity waves on evolution of mesoscale convective systems. *J. Atmos. Sci.*, **77**, 3441–3460, https://doi.org/10.1175/JAS-D-19-0250.1.

——, and R. H. Johnson, 2013: Examination of gravity waves associated with the 13 March 2003 bow echo. *Mon. Wea. Rev.*, **141**, 3735–3756, https://doi.org/10.1175/MWR-D-12-00343.1.

Alexander, M. J., J. R. Holton, and D. R. Durran, 1995: The gravity wave response above deep convection in a squall line simulation. *J. Atmos. Sci.*, **52**, 2212–2226, https://doi.org/10.1175/1520-0469(1995)052<2212:TGWRAD>2.0.CO;2.

——, J. H. Richter, and B. R. Sutherland, 2006: Generation and trapping of gravity waves from convection with comparison to parameterization. *J. Atmos. Sci.*, **63**, 2963–2977, https://doi.org/10.1175/JAS3792.1.

Beres, J. H., 2004: Gravity wave generation by a three-dimensional thermal forcing. *J. Atmos. Sci.*, **61**, 1805–1815, https://doi.org/10.1175/1520-0469(2004)061<1805:GWGBAT>2.0.CO;2.

——, M. J. Alexander, and J. R. Holton, 2004: A method of specifying the gravity wave spectrum above convection based on latent heating properties and background wind. *J. Atmos. Sci.*, **61**, 324–337, https://doi.org/10.1175/1520-0469(2004)061<0324:AMOSTG>2.0.CO;2.

Bretherton, C. S., and P. K. Smolarkiewicz, 1989: Gravity waves, compensating subsidence and detrainment around cumulus clouds. *J. Atmos. Sci.*, **46**, 740–759, https://doi.org/10.1175/1520-0469(1989)046<0740:GWCSAD>2.0.CO;2.

Bryan, G. H., and J. M. Fritsch, 2002: A benchmark simulation for moist nonhydrostatic numerical models. *Mon. Wea. Rev.*, **130**, 2917–2928, https://doi.org/10.1175/1520-0493(2002)130<2917:ABSFMN>2.0.CO;2.

——, J. C. Wyngaard, and J. M. Fritsch, 2003: Resolution requirements for the simulation of deep moist convection. *Mon. Wea. Rev.*, **131**, 2394–2416, https://doi.org/10.1175/1520-0493(2003)131<2394:RRFTSO>2.0.CO;2.

Chun, H.-Y., H.-J. Choi, and I.-S. Song, 2008: Effects of nonlinearity on convectively forced internal gravity waves: Application to a gravity wave drag parameterization. *J. Atmos. Sci.*, **65**, 557–575, https://doi.org/10.1175/2007JAS2255.1.

Du, Y., and R. Rotunno, 2015: Thermally driven diurnally periodic wind signals off the east coast of China. *J. Atmos. Sci.*, **72**, 2806–2821, https://doi.org/10.1175/JAS-D-14-0339.1.

——, and ——, 2018: Diurnal cycle of rainfall and winds near the south coast of China. *J. Atmos. Sci.*, **75**, 2065–2082, https://doi.org/10.1175/JAS-D-17-0397.1.

——, and F. Zhang, 2019: Banded convective activity associated with mesoscale gravity waves over southern China. *J. Geophys. Res. Atmos.*, **124**, 1912–1930, https://doi.org/10.1029/2018JD029523.

——, ——, Y. Q. Sun, J. Wei, and X. Li, 2021: Practical and intrinsic predictability of wave-convection coupled bands over southern China. *J. Geophys. Res. Atmos.*, **126**, e2021JD034882, https://doi.org/10.1029/2021JD034882.

Durran, D. R., 1990: Mountain waves and downslope winds. *Atmospheric Processes over Complex Terrain*, *Meteor. Monogr.*, No. 45, Amer. Meteor. Soc., 59–81, https://doi.org/10.1007/978-1-935704-25-6_4.

Fang, J., and Y. Du, 2022: A global survey of diurnal offshore propagation of rainfall. *Nat. Commun.*, **13**, 7437, https://doi.org/10.1038/s41467-022-34842-0.

Fovell, R. G., 2002: Upstream influence of numerically simulated squall-line storms. *Quart. J. Roy. Meteor. Soc.*, **128**, 893–912, https://doi.org/10.1256/0035900021643737.

——, G. L. Mullendore, and S.-H. Kim, 2006: Discrete propagation in numerically simulated nocturnal squall lines. *Mon. Wea. Rev.*, **134**, 3735–3752, https://doi.org/10.1175/MWR3268.1.

Fritts, D. C., and M. J. Alexander, 2003: Gravity wave dynamics and effects in the middle atmosphere. *Rev. Geophys.*, **50**, 1003, https://doi.org/10.1029/2001RG000106.

Groff, F. P., R. D. Adams-Selin, and R. S. Schumacher, 2021: Response of MCS low-frequency gravity waves to vertical wind shear and nocturnal thermodynamic environments. *J. Atmos. Sci.*, **78**, 3889–3908, https://doi.org/10.1175/JAS-D-20-0208.1.

Haertel, P. T., R. H. Johnson, and S. N. Tulich, 2001: Some simple simulations of thunderstorm outflows. *J. Atmos. Sci.*, **58**, 504–516, https://doi.org/10.1175/1520-0469(2001)058<0504:SSSOTO>2.0.CO;2.

Halliday, O. J., S. D. Griffiths, D. J. Parker, A. Stirling, and S. Vosper, 2018: Forced gravity waves and the tropospheric response to convection. *Quart. J. Roy. Meteor. Soc.*, **144**, 917–933, https://doi.org/10.1002/qj.3278.

Han, J.-Y., and J.-J. Baik, 2009: Theoretical studies of convectively forced mesoscale flows in three dimensions. Part I: Uniform basic-state flow. *J. Atmos. Sci.*, **66**, 947–965, https://doi.org/10.1175/2008JAS2915.1.

——, and ——, 2012: Nonlinear effects on convectively forced two-dimensional mesoscale flows. *J. Atmos. Sci.*, **69**, 3391–3404, https://doi.org/10.1175/JAS-D-11-0335.1.

Jensen, E. J., and Coauthors, 2016: High-frequency gravity waves and homogeneous ice nucleation in tropical tropopause layer cirrus. *Geophys. Res. Lett.*, **43**, 6629–6635, https://doi.org/10.1002/2016GL069426.

Lane, T. P., 2015: Gravity waves: Convectively generated gravity waves. *Encyclopedia of Atmospheric Sciences*, Elsevier, 171–179.

——, and M. J. Reeder, 2001: Convectively generated gravity waves and their effect on the cloud environment. *J. Atmos. Sci.*, **58**, 2427–2440, https://doi.org/10.1175/1520-0469(2001)058<2427:CGGWAT>2.0.CO;2.

——, and T. L. Clark, 2002: Gravity waves generated by the dry convective boundary layer: Two-dimensional scale selection and boundary-layer feedback. *Quart. J. Roy. Meteor. Soc.*, **128**, 1543–1570, https://doi.org/10.1002/qj.200212858308.

——, and F. Zhang, 2011: Coupling between gravity waves and tropical convection at mesoscales. *J. Atmos. Sci.*, **68**, 2582–2598, https://doi.org/10.1175/2011JAS3577.1.

——, M. J. Reeder, and T. L. Clark, 2001: Numerical modeling of gravity wave generation by deep tropical convection. *J. Atmos. Sci.*, **58**, 1249–1274, https://doi.org/10.1175/1520-0469(2001)058<1249:NMOGWG>2.0.CO;2.

Lindzen, R. S., and K.-K. Tung, 1976: Banded convective activity and ducted gravity waves. *Mon. Wea. Rev.*, **104**, 1602–1617,

https://doi.org/10.1175/1520-0493(1976)104<1602:BCAADG>2.0.CO;2.

Mapes, B. E., 1993: Gregarious tropical convection. *J. Atmos. Sci.*, **50**, 2026–2037, https://doi.org/10.1175/1520-0469(1993)050<2026:GTC>2.0.CO;2.

Markowski, P. M., and Y. P. Richardson, 2014: The influence of environmental low-level shear and cold pools on tornadogenesis: Insights from idealized simulations. *J. Atmos. Sci.*, **71**, 243–275, https://doi.org/10.1175/JAS-D-13-0159.1.

McAnelly, R. L., J. E. Nachamkin, W. R. Cotton, and M. E. Nicholls, 1997: Upscale evolution of MCSs: Doppler radar analysis and analytical investigation. *Mon. Wea. Rev.*, **125**, 1083–1110, https://doi.org/10.1175/1520-0493(1997)125<1083:UEOMDR>2.0.CO;2.

Morrison, H., G. Thompson, and V. Tatarskii, 2009: Impact of cloud microphysics on the development of trailing stratiform precipitation in a simulated squall line: Comparison of one- and two-moment schemes. *Mon. Wea. Rev.*, **137**, 991–1007, https://doi.org/10.1175/2008MWR2556.1.

Nicholls, M. E., R. A. Pielke, and W. R. Cotton, 1991: Thermally forced gravity waves in an atmosphere at rest. *J. Atmos. Sci.*, **48**, 1869–1884, https://doi.org/10.1175/1520-0469(1991)048<1869:TFGWIA>2.0.CO;2.

Pandya, R. E., and D. R. Durran, 1996: The influence of convectively generated thermal forcing on the mesoscale circulation around squall lines. *J. Atmos. Sci.*, **53**, 2924–2951, https://doi.org/10.1175/1520-0469(1996)053<2924:TIOCGT>2.0.CO;2.

——, and M. J. Alexander, 1999: Linear stratospheric gravity waves above convective thermal forcing. *J. Atmos. Sci.*, **56**, 2434–2446, https://doi.org/10.1175/1520-0469(1999)056<2434:LSGWAC>2.0.CO;2.

——, D. Durran, and C. Bretherton, 1993: Comments on "Thermally forced gravity waves in an atmosphere at rest." *J. Atmos. Sci.*, **50**, 4097–4101, https://doi.org/10.1175/1520-0469(1993)050<4097:COFGWI>2.0.CO;2.

——, ——, and M. L. Weisman, 2000: The influence of convective thermal forcing on the three-dimensional circulation around squall lines. *J. Atmos. Sci.*, **57**, 29–45, https://doi.org/10.1175/1520-0469(2000)057<0029:TIOCTF>2.0.CO;2.

Plougonven, R., and F. Zhang, 2014: Internal gravity waves from atmospheric jets and fronts. *Rev. Geophys.*, **52**, 33–76, https://doi.org/10.1002/2012RG000419.

Prasad, A. A., S. C. Sherwood, M. J. Reeder, and T. P. Lane, 2019: Rapidly evolving cirrus clouds modulated by convectively generated gravity waves. *J. Geophys. Res. Atmos.*, **124**, 7327–7338, https://doi.org/10.1029/2019JD030538.

Ralph, F. M., V. Venkateswaran, and M. Crochet, 1993: Observations of a mesoscale ducted gravity wave. *J. Atmos. Sci.*, **50**, 3277–3291, https://doi.org/10.1175/1520-0469(1993)050<3277:OOAMDG>2.0.CO;2.

Rotunno, R., J. B. Klemp, and M. L. Weisman, 1988: A theory for strong, long-lived squall lines. *J. Atmos. Sci.*, **45**, 463–485, https://doi.org/10.1175/1520-0469(1988)045<0463:ATFSLL>2.0.CO;2.

Ruppert, J. H., Jr., S. E. Koch, X. Chen, Y. Du, A. Seimon, Y. Q. Sun, J. Wei, and L. F. Bosart, 2022: Mesoscale gravity waves and midlatitude weather: A tribute to Fuqing Zhang. *Bull. Amer. Meteor. Soc.*, **103**, E129–E156, https://doi.org/10.1175/BAMS-D-20-0005.1.

Seo, J. M., J.-J. Baik, and H.-Y. Chun, 2018: Theoretical investigation of nonhydrostatic effects on convectively forced flows: Propagating and evanescent gravity-wave modes. *Phys. Fluids*, **30**, 126604, https://doi.org/10.1063/1.5053444.

Shige, S., and T. Satomura, 2001: Westward generation of eastward-moving tropical convective bands in TOGA COARE. *J. Atmos. Sci.*, **58**, 3724–3740, https://doi.org/10.1175/1520-0469(2001)058<3724:WGOEMT>2.0.CO;2.

Song, I.-S., H.-Y. Chun, and T. P. Lane, 2003: Generation mechanisms of convectively forced internal gravity waves and their propagation to the stratosphere. *J. Atmos. Sci.*, **60**, 1960–1980, https://doi.org/10.1175/1520-0469(2003)060<1960:GMOCFI>2.0.CO;2.

Stechmann, S. N., and A. J. Majda, 2009: Gravity waves in shear and implications for organized convection. *J. Atmos. Sci.*, **66**, 2579–2599, https://doi.org/10.1175/2009JAS2976.1.

Stephan, C. C., M. J. Alexander, M. Hedlin, C. D. de Groot-Hedlin, and L. Hoffmann, 2016: A case study on the far-field properties of propagating tropospheric gravity waves. *Mon. Wea. Rev.*, **144**, 2947–2961, https://doi.org/10.1175/MWR-D-16-0054.1.

Su, T., and G. Zhai, 2017: The role of convectively generated gravity waves on convective initiation: A case study. *Mon. Wea. Rev.*, **145**, 335–359, https://doi.org/10.1175/MWR-D-16-0196.1.

Varble, A., H. Morrison, and E. Zipser, 2020: Effects of underresolved convective dynamics on the evolution of a squall line. *Mon. Wea. Rev.*, **148**, 289–311, https://doi.org/10.1175/MWR-D-19-0187.1.

Wang, Y., L. Zhang, J. Peng, and J. Guan, 2018: Mesoscale gravity waves in the mei-yu front system. *J. Atmos. Sci.*, **75**, 587–609, https://doi.org/10.1175/JAS-D-17-0012.1.

Wei, J., and F. Zhang, 2014: Mesoscale gravity waves in moist baroclinic jet–front systems. *J. Atmos. Sci.*, **71**, 929–952, https://doi.org/10.1175/JAS-D-13-0171.1.

Weisman, M. L., and J. B. Klemp, 1982: The dependence of numerically simulated convective storms on vertical wind shear and buoyancy. *Mon. Wea. Rev.*, **110**, 504–520, https://doi.org/10.1175/1520-0493(1982)110<0504:TDONSC>2.0.CO;2.

Wilson, J. W., S. B. Trier, D. W. Reif, R. D. Roberts, and T. M. Weckwerth, 2018: Nocturnal elevated convection initiation of the PECAN 4 July hailstorm. *Mon. Wea. Rev.*, **146**, 243–262, https://doi.org/10.1175/MWR-D-17-0176.1.